

McGILL UNIVERSITY

MASTERS THESIS

---

**Collinear Laser Spectroscopy on  
Neutron-Rich Rubidium Isotopes and  
Development of a Laser Frequency  
Locking System**

---

*Author:*

Allen LEARY

*Supervisor:*

Dr. Fritz BUCHINGER

*A thesis submitted in partial fulfilment of the requirements  
for the degree of Masters of Science*

*in the*  
Department of Physics

August 2014

© Allen Y. Leary

MCGILL UNIVERSITY

## *Abstract*

Faculty of Science  
Department of Physics

Masters of Science

### **Collinear Laser Spectroscopy on Neutron-Rich Rubidium Isotopes and Development of a Laser Frequency Locking System**

by Allen LEARY

The neutron rich rubidium isotope chain up to  $N=61$  is investigated using collinear fast-beam laser spectroscopy (CFBS) at the ISAC radioactive ion beam facility at TRIUMF. These measurements extend and update the comprehensive study of the rubidium isotopes chain undertaken by Thibault et al. Updated changes in mean square charge radii values across the chain are computed using the latest atomic factors for the rubidium  $D_2$  line and their trends with respect to nuclear deformation discussed. Equally the existence of a long lived isomeric state at  $N=61$  is confirmed. A low spin state is assigned a spin of  $I=0$  and a high spin state is tentatively assigned a spin of  $I=3$  based on this analysis and gamma decay results.

These measurements have been carried out in conjunction with the development of a laser frequency locking program and the characterization of the confocal Fabry Perot etalon employed by the CFBS group. This program guarantees the stability of the laser frequency to a dither of 2MHz during laser spectroscopy experiments, therefore reducing the errors associated to the measurements of hyperfine structure and isotope shift undertaken by the CFBS group.

---

# Resume

La chaîne d'isotopes de rubidium riche en neutron jusqu'à  $N=61$  est étudiée en utilisant la spectroscopie collinéaire de fluorescence rapide (CFBS) au centre d'isotopes radioactif ISAC à TRIUMF. Ces résultats mettent à jour ceux obtenus auparavant par Thibault et al. De nouvelles calculations des propriétés du rayon de charge sont faites à l'aide des plus récents résultats pour les facteurs atomiques du rubidium. Les tendances de ces nouveaux résultats sont également présentées dans le contexte de l'évolution des formes nucléaires. L'existence d'un état isomérique de longue période de vie est également confirmée pour  $N=61$ . L'état au spin inférieur est assigné  $I=0$  tandis que celui au spin supérieur est provisoirement assigné  $I=3$  basé sur l'analyse de ces résultats.

En parallèle à ces résultats, le développement d'un programme pour stabiliser la fréquence et la calibration du Fabry Perot utilisé par CFBS sont présentés. Ce programme garantit la stabilité du laser jusqu'à 2 MHz lors des expériences de spectroscopie. Ceci permet de réduire les erreurs associées à la mesure de la structure hyperfine et du décalage isotopique pris en compte par le groupe CFBS.

## *Acknowledgements*

This thesis may bear my name but it is the result of a collaboration of a great many individuals without which none of this could have been achieved. I will be forever thankful of the opportunity afforded to me by Dr. Fritz Buchinger to pursue this Master's degree at TRIUMF and expand my scientific knowledge far beyond the scope of the PHYS 439 lab you supervised in my undergraduate. I am equally thankful for all the assistance and insight provided to me by Prof. John Crawford who shed much light on the dark art that is hyperfine peak fitting.

I have been most fortunate to work under the omniscient Dr. Matt Pearson whilst at TRIUMF, who has taught me all I know about laser spectroscopy. The laser frequency locking program is his brainchild, I am merely translating it into script to the best of my ability but I am sure much got lost in translation. I would like to sincerely thank Dr. Tom Proctor whose invaluable assistance and insight is generously scattered across this thesis. Your promising career in professional football may have been cruelly cut short but I think the fame and glory of physics will provide ample solace.

I would like to equally thank my extensive network of family support that has been there for me through thick and thin. In particular my mother who was my very first academic mentor, a role she has never fully relinquished, my father who I still don't think fully understands why I willingly signed up for this whole academia business but has always been very supportive of it. My aunt who has been my cultural and artistic influence that counter-balances my scientific pursuits and promotes my prolonged sanity. My brother that may be categorized as marginally smarter than me according to some standardized tests has always been an invaluable source of motivation and pride.

Last but not least I would like to thank Mickaela Nixon, that has been there for me from the start of my time at McGill and has seen me all the way through. Without her none of this could have happened. I cant wait to see you on the other side my love.

# Contents

<b>Abstract</b>	<b>i</b>
<b>Acknowledgements</b>	<b>iii</b>
<b>Contents</b>	<b>iv</b>
<b>List of Figures</b>	<b>vi</b>
<b>List of Tables</b>	<b>vii</b>
<b>Abbreviations</b>	<b>ix</b>
<b>1 Introduction</b>	<b>1</b>
1.1 General Overview of Laser Spectroscopy in Nuclear Physics . . . . .	1
1.2 This Work . . . . .	3
<b>2 Spectroscopy and Nuclear Properties</b>	<b>5</b>
2.1 Spectroscopy . . . . .	5
2.1.1 Introduction to Spectroscopy . . . . .	5
2.1.2 Spectroscopic Observables . . . . .	6
2.1.2.1 Fine and Hyperfine Spectral lines . . . . .	6
2.1.2.2 Isotope Shifts . . . . .	12
2.2 Nuclear Properties . . . . .	14
2.2.1 Nuclear Moments and Spin . . . . .	15
2.2.2 Mean Square Charge Radius and Shape . . . . .	17
<b>3 Experimental Methods of Collinear Fast Beam Spectroscopy</b>	<b>20</b>
3.1 Radioactive Ion Production at TRIUMF . . . . .	20
3.2 The CFBS Beamline . . . . .	21
3.2.1 Collinear Laser Spectroscopy . . . . .	21
3.2.2 Radio Frequency Quadrupole and Light Interaction Region . . . . .	23
3.2.3 The Laser System . . . . .	26
3.2.4 Laser Chopping with an EOM . . . . .	28
3.3 Data Acquisition . . . . .	30
3.3.1 Shape and Width of Spectral Lines . . . . .	30
3.3.2 Isotope Shift Measurements . . . . .	32

---

3.3.3	An MCS DAQ system . . . . .	33
<b>4</b>	<b>Laser Spectroscopy on Neutron Rich Rubidium</b>	<b>37</b>
4.1	Physical Properties . . . . .	37
4.2	Extension of previous studies of the rubidium isotope chain . . . . .	38
4.2.1	Previous work and motivations . . . . .	38
4.2.2	Recent extensions in measures of MSCR . . . . .	39
4.3	The neutron-rich rubidium program at TRIUMF and its findings . . . . .	41
<b>5</b>	<b>Laser Locking Program</b>	<b>48</b>
5.1	Motivation and Overview . . . . .	48
5.2	Frequency stabilization apparatus . . . . .	49
5.3	Laser Locking with LabView: Data acquisition and feedback control . . . . .	54
5.4	Performance of the laser stabilization system . . . . .	58
5.4.1	The free spectral range of the confocal Fabry-Perot . . . . .	58
5.4.2	Stability of Laser Locking Program . . . . .	62
5.4.3	Conclusion and Outlook . . . . .	65

# List of Figures

2.1	Hyperfine lines and their corresponding peaks in the frequency spectrum .	7
2.2	Mechanism of nuclear absorption and fluorescence emission to probe energy levels . . . . .	8
2.3	Illustration of Isotope Shift . . . . .	13
3.1	Overview of the CFBS experiment beamline . . . . .	22
3.2	RFQ Overview . . . . .	24
3.3	Diagram of the Laser System for CFBS . . . . .	27
3.4	Illustration of the cycling transition and optical pumping for the high spin case . . . . .	29
3.5	DAQ block diagram . . . . .	34
3.6	Triggering and Pulse Sequence for the MCS-DAQ system . . . . .	36
4.1	Changes in Mean Square Charge Radii . . . . .	39
4.2	Reevaluated MSCR for the rubidium chain compared to previous computations. . . . .	41
4.3	Optical spectrum for $^{98}\text{Rb}$ , measured on the D2 transition with associated fits. . . . .	46
5.1	The schematic diagram of the locking apparatus . . . . .	50
5.2	Diagram of the confocal Fabry Perot and the path taken by the light in its cavity . . . . .	51
5.3	Typical output spectrum of the CFP and illustration of FSR, FWHM. . .	52
5.4	Block Diagram of the LabView Laser Locking Program which controls cavity scans, data acquisition and laser frequency . . . . .	56
5.5	Illustration of AOM generated sidebands . . . . .	59
5.6	Fitting the overlapping HeNe sidebands peaks to extract centroid position	60
5.7	Sideband intercept with associated linear fits used to determine FSR . . .	61
5.8	Drift of the HeNe sidebands . . . . .	63
5.9	Drift of the unlocked MBR . . . . .	64
5.10	Drift of the locked MBR . . . . .	65

# List of Tables

4.1	A and B hyperfine coefficients and quadrupole moments extracted by Thibault et al . . . . .	42
4.2	Isotope shift, change in mean squared charge radius and estimated deformation parameters for rubidium isotopes . . . . .	43
4.3	Theoretical predictions for neutron rich rubidium chain . . . . .	44
4.4	$^{98}\text{Rb}$ experimental measured hyperfine A and B coefficients, isotope shifts and associated $\chi_r^2$ . . . . .	47

*À la Mémoire de* 爷爷

# Abbreviations

<b>TRIUMF</b>	Tri-University Meson Facility
<b>ISAC</b>	Isotope Separator and Accelerator
<b>CFBS</b>	Collinear Laser Spectroscopy
<b>HFS</b>	Hyperfine Structure
<b>MSCR</b>	Mean Square Charge Radius
<b>NMS</b>	Normal Mass Shift
<b>SMS</b>	Specific Mass Shift
<b>MCP</b>	Multi-Channel Plate
<b>RFQ</b>	Radio Frequency Quadrupole
<b>LIR</b>	Light Interaction Region
<b>PMT</b>	Photo-Multiplier Tube
<b>MBR</b>	Monolithic Bloc Resonator
<b>HeNe</b>	helium-neon
<b>EOM</b>	Electro-Optical Modulator
<b>CW</b>	Continuous Wave
<b>Rb</b>	rubidium
<b>FWHM</b>	Full Width Half Maximum
<b>MCS</b>	Multi-Channel Scalar
<b>DVM</b>	Digital Voltmeter
<b>DAQ</b>	Data Acquisition
<b>TOF</b>	Time of Flight
<b>PPG</b>	Pulse Programmable Gate
<b>HS/LS</b>	High Spin/Low Spin
<b>LLP</b>	Laser Locking Program
<b>CFP</b>	Confocal Fabry Perot

<b>FSR</b>	Free Spectral Range
<b>PZT</b>	Piezo-Electric Transducer
<b>L</b>	Cavity Length
<b>SP</b>	Set Point
<b>P controller</b>	Proportional Controller
<b>PI controller</b>	Proportional-Integral Controller
<b>NI</b>	National Instruments
<b>DAC</b>	Digital to Analog Converter
<b>ADC</b>	Analog to Digital Converter
<b>DC</b>	Direct Current
<b>RF</b>	Radio Frequency
<b>LLP</b>	Laser Locking Program

# Chapter 1

## Introduction

### 1.1 General Overview of Laser Spectroscopy in Nuclear Physics

The structure of matter and its base constituents has long been subject of discussion and debate but due to the inherent difficulties linked to the study of such small elements it is not until the end of the 20th century that the nucleus was discovered. The birth of nuclear physics, the scientific study of the nucleus is often associated with the work of the English physicist J. J. Thompson, who in 1897 postulated the existence of electrons as a result of his studies of cathode rays [1]. As a result, in 1904 he developed his model for the atom structure in order to add the electron to the atomic model [2]. In his model, negatively charged electrons sat in a cloud of positively charged matter that constituted an electrically neutral atom. This model was soon disproved in 1911 by E. Rutherford's interpretation [3] of the 1909 gold foil experiment undertaken by H. Geiger and E. Marsden [4] under his supervision. The Rutherford model is the first to possess a high mass and charge density core that has come to be named the nucleus, surrounded by orbiting electrons. This model and its proposed nucleus led to the birth of nuclear physics. The new field was quickly subject to much scientific interest and as a result saw rapid evolution of the understanding of the nucleus through both experimental investigations and theoretical studies.

When investigating atomic spectra using spectroscopy, a frequency shift of the center of

gravity is observed from isotope to isotope. This shift is called the isotope shift. In 1913 N. Bohr proposed a formula for the isotopic shift of spectral lines [5]. He postulated that they were a result of recoil kinetic motion of the electron orbits' when subject to different nuclear masses. This effect, now called the mass shift had long been seen in atomic spectral lines of different elements but yet to be explained. When the isotope shift was experimentally found to be of greater magnitude than the proposed mass shift [6] could account for another component of the isotope shift was proposed. This new component, called the field shift arose as a result of the size and shape of the nucleus [7, 8]. Combining these two components along with subsequent investigations has given modern nuclear physics a good understanding of the isotope shift, its origins and how it can be used to study nuclear structure. As a result the change mean square charge radius of the nucleus can be inferred from isotope shift measurements.

Alongside the study of isotope shift, the study of the splitting of spectral lines equally had a bearing on the understanding of nuclear structure. The hyperfine structure as it came to be known causes a splitting of a spectral line where several components are visible for a single atomic transition. They were first observed by Michelson in 1892 [9] but understood much later. An initial proposal to explain these effects was put forward in 1924 by Pauli [10] who suggested they were a result of different couplings of nuclear spin with the total angular momentum of the electrons which produced an angular momentum on the atom. A comprehensive understanding on the origin of these hyperfine splittings was only proposed in 1931 by Schuler [11] who explained how the coupling of the nuclear and electron angular momenta create different shifts in the energy levels of the electron orbits. This hyperfine structure and their associated spectral line splittings are today used to investigate nuclear moments and spin and give nuclear physicists a high resolution tool to investigate nuclear properties.

With the growing understanding of isotope shifts and hyperfine structures and how they related to nuclear structure many experiments were developed to measure them. These measurements yield information on nuclear spin, moments and mean square charge radius. One such experimental tool is optical spectroscopy, which studies the spectra of radiated energy from matter. In order to probe the small energy shifts of the hyperfine structure and the isotope shifts, a high precision stable, controllable light was needed. This tool was the stabilized laser whose invention in the 1970s greatly advanced the

field of spectroscopy. Stabilized lasers can produce narrow bandwidth light which is monochromatic down to few MHz, ideal for investigating hyperfine lines. This allowed for the investigation of long lived and abundant isotopes at room temperature in vapour cells. These isotopes have been extensively studied and their properties reported to the nuclear chart. The focus of nuclear structure research has shifted to increasingly unstable isotopes which are often rarer and short lived. For this reason radioactive ion beam facilities such as ISOLDE, ISAC and many others have made these exotic regions available for investigation using laser spectroscopy. These facilities generally create these rare isotopes by bombarding high energy protons on targets. These high energy and often short lived radioactive elements can no longer be contained in vapour cells and so are sent to laser spectroscopy experiments in high vacuum beam-lines where it is overlapped with the scanning laser used to excite the hyperfine transitions. Another advantage of these on-line experiments at radioactive ion beam facilities is versatility of the experimental set up. The facilities can produce a chain of isotopes for laser spectroscopy to easily investigate isotope shifts along with hyperfine structures.

After several decades of development, laser spectroscopy is still one of the leading techniques for the investigation of nuclear structure. Improvements on radioactive beam production and yields along with sensitivity of detectors and stability of lasers allow for many exotic nuclei to be investigated using laser spectroscopy. The results can be used to further our understanding of nuclear theory.

## 1.2 This Work

This M.Sc thesis will report on the contributions of the author while part of the collinear fast-beam spectroscopy (CFBS) group at TRIUMF. Specifically the work done in this thesis centres on the investigation of neutron rich rubidium isotopes which has been the subject of prolonged scrutiny at TRIUMF for the past couple of years. The element is of interest due to its high degree of deformation for isotopes with higher neutron density than the stable  $^{85}\text{Rb}$  and  $^{87}\text{Rb}$  isotopes. Particular emphasis is placed the  $^{98}\text{Rb}$  isotope of which two coexisting shape isomers are confirmed and nuclear properties extracted.

The last chapter of the thesis is dedicated to the development of a new laser frequency

---

locking program by the author for the CFBS group. The implementation of this program along with the calibration of the laser locking system aims to improve the frequency stability of the laser used to investigate hyperfine structures. By improving this system it is hoped that the errors on the CFBS groups measurements of hyperfine structure will be reduced leading to more precise measurements of nuclear properties.

## Chapter 2

# Spectroscopy and Nuclear Properties

### 2.1 Spectroscopy

#### 2.1.1 Introduction to Spectroscopy

Spectroscopy is the study of the interaction of matter and radiated energy. It is a powerful tool that has allowed many invaluable insights into the properties of light, molecules and atoms. Most of what is known about the internal structure and compositions of atoms and molecules comes from studying their interactions with electromagnetic radiation.

Spectroscopy in quantum mechanical systems such as atoms relies on the coupling of two level quantum mechanical stationary states, via an oscillatory source of energy such as a photon. The coupling of the two states is strongest when the energy of the source matches the energy difference between the two states. It is this maximum coupling that gives rise to resonance peaks in frequency spectrums. The energy  $E$  of a photon is related to its frequency  $\nu$  and wavelength  $\lambda$  by:

$$E = h\nu \tag{2.1a}$$

$$\nu = \frac{c}{\lambda} \tag{2.1b}$$

where  $h$  is Planck's constant and  $c$  the speed of light. A spectrum of the system response against photon frequency will peak at the resonant frequency or energy.

Initial spectroscopic investigations [12] of atoms used gas discharge lamps such as sodium lamps which produced several narrow absorption lines on the visible spectrum corresponding to coarse  $D_2$  line transitions of order 1-10 eV. The sodium  $D_2$  line is equal to 2.104428981(77)eV [13]. As spectroscopic techniques improved, these  $D_2$  lines were found to be composed of further extremely close and fine absorption lines dubbed fine structure, of order  $10^{-5}$  to  $10^{-4}$ eV. These fine structure energy splittings were then found themselves to be composed of a further subset of energy splittings when the nuclear spin of the nucleus was non-zero. These splittings of the fine structure were dubbed the *hyperfine structure*. These hyperfine splittings can be investigated using narrow width laser spectroscopy to probe nuclear structure. They are the finest energy spacings of atomic electron energies known to date and are of the order  $10^{-7} - 10^{-8}$ eV.

### 2.1.2 Spectroscopic Observables

Using spectroscopy to produce frequency spectra such as shown in Figure 2.1, a set of observables are available. These observables allow us to understand and characterize the structure of the nucleus. The range of observables available to laser spectroscopy are discussed in the following section.

#### 2.1.2.1 Fine and Hyperfine Spectral lines

The advance of quantum mechanics and models for atomic structure have shown that electrons exist in discrete energy levels in the atom. The atom's electrons occupy either a ground state configuration or a series of excited states. It is these excited states that produce the resonance peaks in experimental frequency spectra. When an electron is in an excited state it will undergo de-excitation with a characteristic lifetime and emit a discrete quantum of energy in the form of a fluorescence photon as shown in Figure 2.2. This photon will have a wavelength corresponding to the difference in energy between the electronic excited state and the ground state. As the energy levels of the atomic electrons are a result of the unique nuclear electromagnetic interactions they constitute a set of discrete spectral lines which can be seen as a fingerprint proper to each atom.

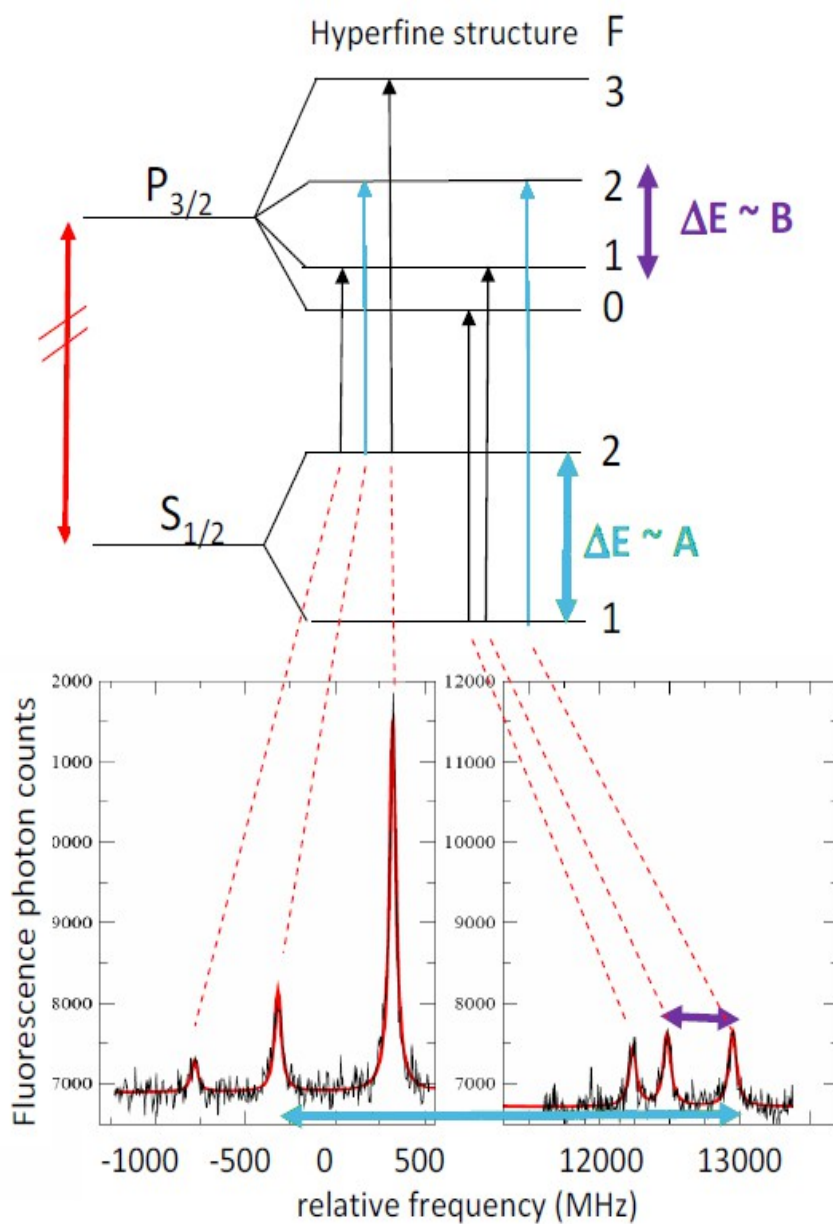


FIGURE 2.1: Diagram illustrating the hyperfine splitting lines (top) and their corresponding peaks in the frequency spectrum as seen during a laser spectroscopy experiment (bottom)

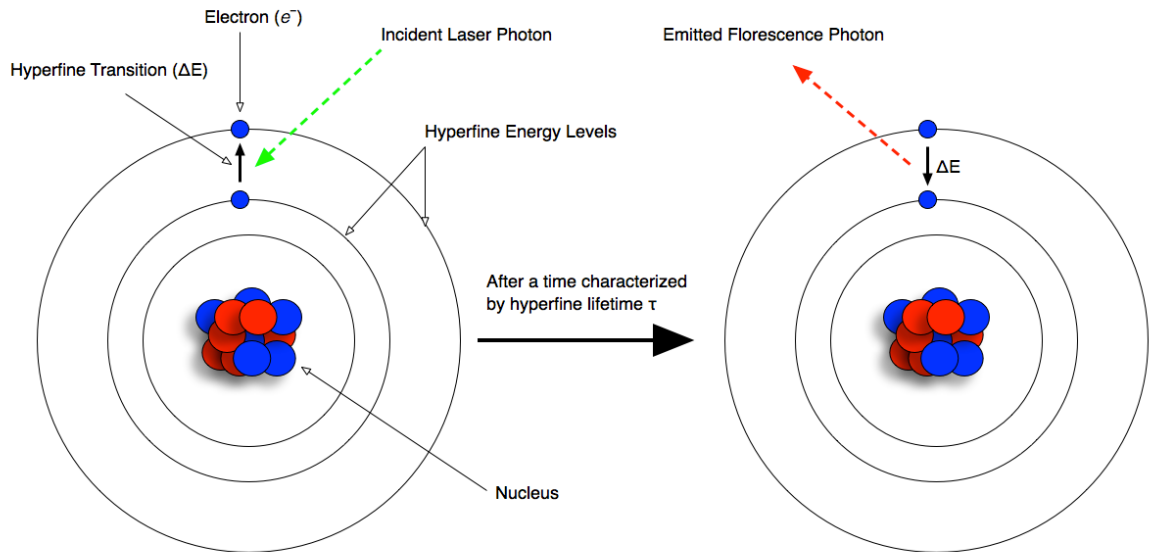


FIGURE 2.2: Mechanism of nuclear absorption and fluorescence emission to probe energy levels

The reason the fine and hyperfine energy splittings were only later discovered was due to their extremely narrow energy spread which required detection techniques with better resolution as opposed to those used for broader spectral lines. The fine structure can be decomposed into three contributions to the Hamiltonian  $H_{fs}$  of the atomic system [14]:

$$H_{fs} = H_0 + H_T + H_D + H_{s-o} \quad (2.2)$$

With  $H_0$  the non-relativistic quantum prediction,  $H_T$  the relativistic correction to kinetic energy,  $H_D$  the Darwin term from the non relativistic correction of the Dirac equation and finally  $H_{s-o}$  the spin-orbit coupling term which gives rise to the degeneracy of the energy levels seen in the fine structure.  $H_{s-o}$  arises from the interaction of the magnetic field of the nucleus felt by the orbiting electron and the electron's magnetic moment due to its intrinsic angular momentum or spin. The two magnetic vectors couple in such a way that there is a certain energetic penalty given to their different orientations.

This gives rise to the spin orbit energy correction, which is dependent on the angular momentum quantum numbers L (orbital) and S (spin) of the form:

$$\Delta E_{s-o} \propto \vec{L} \cdot \vec{S} \quad (2.3)$$

Given that the electron can have spin up or down this energy splitting gives two fine structure lines.

The hyperfine structure is typically orders of magnitude smaller than the fine structure and results from interactions of the nucleus with internally generated electric and magnetic fields. The hyperfine structure can be decomposed into two contributions to its Hamiltonian  $H_{hfs}$ , one magnetic and one electric:

$$H_{hfs} = H_B + H_E \quad (2.4)$$

The magnetic contribution  $H_B$  is due to the interaction between the nuclear magnetic dipole  $\mu_I$  and the magnetic field  $B_e$  of the distribution of orbiting electrons.  $\mu_I$  results from the total angular momentum  $\vec{I}$  of the nucleus which is a sum of angular momenta of all the nucleons that constitute it. It has the form:

$$\mu_I = g_I \mu_N \vec{I} \quad (2.5)$$

where  $g_I$  is the g-factor and  $\mu_N$  the nuclear magneton.

The magnetic field felt by an orbiting electron  $B_e$ , is a product of the collective motion of all the atomic electrons which is associated with the orbital (L) and spin (S) angular momenta of the electrons. It can be decomposed into two components  $\vec{B}_L$  and  $\vec{B}_S$ . The magnetic contribution to the hyperfine splittings can be written as:

$$H_B = \vec{\mu}_I \cdot (\vec{B}_L + \vec{B}_S) \quad (2.6a)$$

$$= -\vec{\mu}_I \cdot \vec{B}_e \quad (2.6b)$$

Electron orbital angular momentum results from the motion of the electron about the fixed stationary nucleus. The magnetic field  $B_l$  at the nucleus due to a single electron

of charge  $e$  and distance  $r$  is given by[15]:

$$\vec{B}_l = -2\mu_B \frac{\mu_0}{4\pi r^3} \vec{l} \quad (2.7)$$

with  $\mu_0$  the vacuum permeability constant,  $\mu_B$  the Bohr magneton.

Most atoms have multiple orbiting electrons and so the magnetic field  $\vec{B}_L$  can be rewritten as a function of the total orbital angular momentum  $\vec{L}$  and by summing over the electrons such that:

$$\vec{B}_L = -2\mu_B \frac{\mu_0}{4\pi} \frac{1}{L_z} \sum_i \frac{\hat{l}_{zi}}{\hat{r}_i^3} \vec{L} \quad (2.8)$$

with  $\sum_i \frac{\hat{l}_{zi}}{L_z} \vec{L}$  the sum over electron orbital angular momenta using a projection along the z axis.

Electron spin is an intrinsic angular momentum associated to the charged electron which results in a magnetic dipole moment. This dipole moment is the source of a magnetic field. An electron with spin  $\vec{s}$  has magnetic moment  $\vec{\mu}_s^e$  of the form:

$$\vec{\mu}_s^e = -g_s \mu_B \vec{s} \quad (2.9)$$

with  $g_s$  the electron g-factor. The magnetic field of the electron dipole moment can be written in function of  $\vec{\mu}_s^e$  as [16]:

$$\vec{B}_s = \frac{\mu_0}{4\pi r^3} [3(\vec{\mu}_s^e \cdot \hat{r})\hat{r} - \vec{\mu}_s^e] + \frac{2}{3}\mu_0 \delta^3(r) \vec{\mu}_s^e \quad (2.10)$$

with  $\delta^3(r)$  the three dimensional Dirac delta function as electrons are considered as point-like sources. The relative size of the nucleus with respect to electrons make this a good approximation.

The electric contribution  $H_E$  to the hyperfine splittings arises if the nucleus does not have a spherically symmetric charge distribution. As nuclei increase in size given additional protons and neutrons, they have increasingly complicated nucleus structures and shapes due to the change in nuclear potential. A deformed nucleus has as a result a non-zero electric quadrupole moment  $Q_l$ . The electric n-poles from the multipole expansion of a sphere are used to quantify deformation [17]:

$$Q_l = \int d^3r r^l P_l(\cos\theta) \phi(r) \quad (2.11)$$

Where  $P_l(\cos\theta)$  is the Legendre polynomial of degree  $l$  and  $\phi(r)$  the charge distribution of the nucleus at distance  $r$  from its centre. The electric quadrupole moment corresponds to the  $l = 2$  case such that:

$$Q_2 = \frac{1}{e} \int d^3r \rho(\vec{r}) [3z^2 - r^2] \quad (2.12)$$

with  $z$  the axis of elongation of the deformation.  $Q_2$  will be zero if the nucleus is perfectly spherical. Commonly used parametrization allows us to compute these  $Q_2$  terms using spherical harmonics. The series is infinite but only the first couple of terms are relevant when computing the quadrupole moment. Assuming the spherical deformation is volume conserving [18] the shape of the charge distribution can be represented by the parametrization:

$$R(\theta) = \left[ 1 + \sum_{n=2}^n \left( \beta_n Y_{n0}(\theta, 0) - \frac{\beta_n^2}{4\pi} \right) \right] \quad (2.13)$$

with  $\beta_n$  the deformation parameter of order  $n$ .

Considering the spherical harmonics  $Y_{n,\phi}(\theta, \phi)$  to be symmetric in cylindrical coordinates eliminates the  $\phi$  dependency. So the multipole expansion  $Q_l$  can be written using this parametrization:

$$Q_l = \frac{3}{8\pi} m_{nucleus} R(\theta) \quad (2.14)$$

with  $m_{nucleus}$  the mass of the nucleus.

The electric quadrupole moment can be written as a function of the  $\beta_n$  expansion coefficients, whilst numerically evaluating the spherical harmonics  $Y_{lm}$  in such a way that we are left with [19]:

$$Q_2 \approx \frac{5Z \langle r_{sph} \rangle^2}{\sqrt{5\pi}} \langle \beta_2 \rangle (1 + 0.36 \langle \beta_2 \rangle) \quad (2.15)$$

with the expansion only evaluated for  $n=2$  as higher order terms consist of vanishing contributions.  $\langle r_{sph} \rangle^2$  is the mean square charge radius of the perfect spherical nucleus which can be deformed by nonzero  $\langle \beta_2 \rangle$  terms. Positive  $\langle \beta_2 \rangle$  indicates prolate deformation and negative  $\langle \beta_2 \rangle$  arise from oblate deformations. The electric contribution to the hyperfine structure Hamiltonian is the quadrupole moment multiplied by the electric field gradient such that

$$H_E = eQ_2 \frac{\delta^2 V}{\delta z^2} \quad (2.16)$$

So we now have the full expression for  $H_{hfs}$  and understand the origins of the energy

splittings. By measuring the hyperfine splittings along with knowledge of their mechanism allows the extraction of nuclear properties.

### 2.1.2.2 Isotope Shifts

When comparing the spectral lines originating from atoms whose nuclei differ only in the number of neutrons (isotopes of the same element), effects due to the finite mass and volume of the nucleus become apparent. Unaffected by the hyperfine structure (by taking the centre of gravity of the observed splitting), the spectral lines of different isotopes vary depending on the effect of the neutron on the nucleus.

The centroid shift between two isotopes is referred to as the isotope shift  $\delta\nu^{A,A'}$  with  $A$  the reference isotope. It is observed to have both positive and negative values. For isotopes of atomic number  $A$  and  $A'$  and for a given transition frequency it has the form:

$$\delta\nu^{A,A'} = \nu^A - \nu^{A'} \quad (2.17)$$

An illustration of the isotope shift in the context of s to p transition frequencies can be seen in Figure 2.3. It has two components: a mass shift  $\delta_{ms}^{A,A'}$  which is a kinematic effect due to the change in nuclear mass and a field shift  $\delta_{fs}^{A,A'}$  which is due to the perturbation of electronic orbitals by the modification of the shape of the nuclear potential. The mass shift is itself composed of two contributions, the Normal Mass Shift (NMS) and the Specific Mass Shift (SMS) such that [20]:

$$\delta_{ms}^{A,A'} = \delta_{NMS}^{A,A'} + \delta_{SMS}^{A,A'} \quad (2.18a)$$

$$= \left( \frac{1}{m_A} - \frac{1}{m_{A'}} \right) (N + S) \quad (2.18b)$$

with  $N$  and  $S$  the normal and specific mass shift constants. The normal mass shift constant has the form  $N = \nu m_e / m_u$  (with  $m_u$  the atomic mass unit,  $\nu$  the transition frequency and  $m_e$  the mass of the electron). The NMS contribution resulting from nucleus-electron interactions can be calculated but the SMS due to the inter electronic correlations require complex calculations which become increasingly challenging for heavier elements. Therefore they have to be inferred from isotope chains empirically [21].

The variation in neutron number from isotope to isotope changes the nuclear charge distribution which in turn changes the nuclear potential. This is reflected in the field

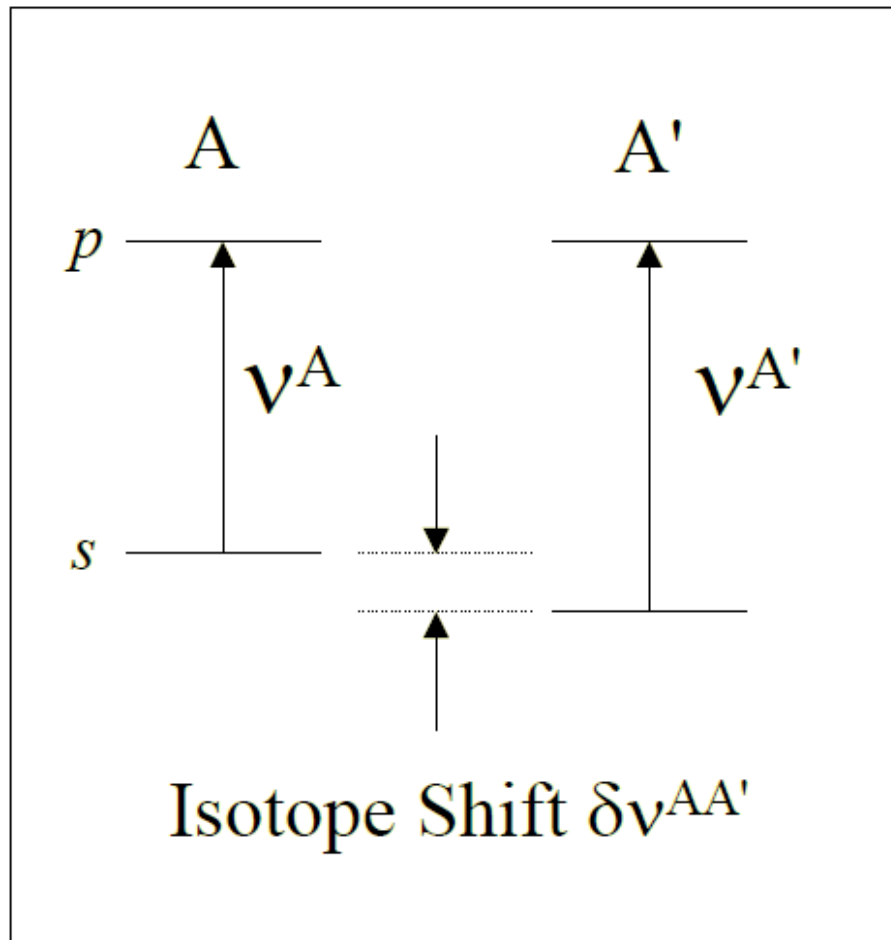


FIGURE 2.3: Isotope Shift shown in the transition lines between elements of atomic number A and A'

shift as a function of the change in mean square charge radius  $\delta\langle r^2\rangle^{A,A'}$ . The energy shift results from the overlap of the electron's wave function  $\psi_e(r)$  and the nucleus. It can be expressed as [20]:

$$\delta E = e \int_0^\infty \psi_e^*(r) \delta V(r) \psi_e(r) d^3r \quad (2.19)$$

The integral is carried out over the volume of the nucleus with  $\delta V(r)$ , the difference between Coulomb potentials results in [7, 19] :

$$\delta\nu_{fs}^{A,A'} = \frac{a_0^3\pi}{Z}\beta_s\Delta|\psi_e(0)|^2 f(Z)\delta\langle r^2\rangle^{A,A'} \quad (2.20a)$$

$$= F_{el}\lambda^{A,A'} \quad (2.20b)$$

with  $a_0$  the Bohr radius,  $Z$  the atomic number,  $\beta_s$  an electronic shielding factor due to the other atomic electrons and  $\Delta|\psi_e(0)|^2$  the change of electron wave function evaluated at the centre of the nucleus. The electronic factor  $F_{el}$  and the Seltzer moment  $\lambda^{A,A'}$  are described as:

$$F_{el} = \frac{a_0^3\pi}{Z}\beta_s\Delta|\psi_e(0)|^2 f(Z) \quad (2.21a)$$

$$\lambda^{A,A'} = \delta\langle r^2\rangle^{A,A'} + \frac{C_2}{C_1}\delta\langle r^4\rangle^{A,A'} + \frac{C_3}{C_1}\delta\langle r^6\rangle^{A,A'} + \dots \quad (2.21b)$$

The Seltzer factor takes into account the higher order radial moments [22] due to the non uniformity of the electron wavefunction across the nuclear charge distribution for heavy nuclear systems. Higher order terms decrease rapidly and are small in comparison with  $\delta\langle r^2\rangle^{A,A'}$  in such a way that we can approximate :  $\lambda^{A,A'} \approx \delta\langle r^2\rangle^{A,A'}$ . This is due to the effects being negligible to the laser resolution. Generally in alkalines, the  $D_2$  electronic transition between  $S_{\frac{1}{2}}$  and  $P_{\frac{3}{2}}$  are used to study isotope shift and give insights into the nuclear core. Putting these elements together the total isotope shift can be written as :

$$\delta\nu_{IS}^{A,A'} = K_{MS}\frac{m_{A'} - m_A}{m_A m_{A'}} + F_{el}\delta\langle r^2\rangle^{A,A'} \quad (2.22)$$

With  $K_{MS} = (N + S)$  the mass shift factor and  $F_{el}$  the field shift factor.

## 2.2 Nuclear Properties

The origin of the hyperfine structure being understood, coupled with laser spectroscopy spectroscopy allows us to link the experimental data with our quantum mechanical understanding of the nucleus in order to deduce nuclear structure properties.

### 2.2.1 Nuclear Moments and Spin

As previously seen the hyperfine structure and its associated energy splittings are due to the magnetic and electric interactions between atomic electrons and the nucleus. The magnitude of the energy shifts can be computed by taking the expectation value of the perturbed hyperfine Hamiltonians. The magnetic component  $H_B$  can be rewritten in terms of the operator for nuclear spin  $\hat{I}$ , the operator for total electronic orbital angular momentum  $\hat{J}$  and the magnetic field at the nuclear site due to the atomic electrons  $B_e(0)$  such that [23]:

$$H_B = -\frac{\mu B_e(0)}{I J} \hat{I} \cdot \hat{J} \quad (2.23a)$$

$$= A \hat{I} \cdot \hat{J} \quad (2.23b)$$

with  $A = \frac{\mu B_e(0)}{I J}$  the hyperfine parameter which allows us to approximate nuclear magnetic dipole moment  $\mu$ . The product of the angular momentum operators can be evaluated using  $\hat{F}^2 = (\hat{I} + \hat{J})^2 = \hat{I}^2 + 2\hat{I} \cdot \hat{J} + \hat{J}^2$  such that the expectation value of the operator product is:

$$\langle I J F m_F | \hat{I} \cdot \hat{J} | I J F m_F \rangle = \frac{1}{2} [F(F+1) - J(J+1) - I(I+1)] \quad (2.24)$$

And so the energy shift  $\Delta E_B$  for  $I \geq 1/2$  is given by the expectation value of  $H_B$  such that:

$$\Delta E_B = \langle I J F m_F | H_B | I J F m_F \rangle \quad (2.25a)$$

$$= A \frac{[F(F+1) - J(J+1) - I(I+1)]}{2} \quad (2.25b)$$

$$= \frac{A}{2} K \quad (2.25c)$$

With  $K = [F(F+1) - J(J+1) - I(I+1)]$

By evaluating the expectation value for  $H_E$  we can obtain the energy splittings issue from the electric component. It can be shown that [24]:

$$\Delta E_E = \langle I J F m_F | H_E | I J F m_F \rangle \quad (2.26a)$$

$$= \frac{B}{4} \frac{\frac{3}{2} K(K+1) - 2IJ(I+1)(J+1)}{IJ(2I-1)(2J-1)} \quad (2.26b)$$

where  $B = eQ \langle (\frac{\partial V}{\partial z})^2 \rangle$  is the hyperfine coefficient relating to the quadrupole moment and  $\langle (\frac{\partial V}{\partial z})^2 \rangle$  is the average change of the electric field gradient of the atomic electrons at the nucleus. When we have a perfectly spherical charge distribution this term is equal to zero and there is no contribution from the electric quadrupole moment to the hyperfine splittings.

It is important to note that computing the electromagnetic field generated by the atomic electrons needed for the  $B$  coefficient is quite challenging as is computing the magnetic field at the nuclear site due to atomic electrons needed for the  $A$  coefficient. In order to overcome this limitation a fully and precisely characterized reference isotope is employed using the same atomic transition in order to extract the coefficients of the isotope of interest such that:

$$\frac{A_{ref}}{A} = \frac{\mu_{ref}}{\mu} \frac{I}{I_{ref}} \quad (2.27a)$$

$$\frac{B_{ref}}{B} = \frac{Q_{ref}}{Q} \quad (2.27b)$$

Combining the energy splitting contributions of both the magnetic and electric components and applying them to the coarser fine structure, the energy splittings are [17]:

$$\Delta E_{hfs} = \Delta E_B + \Delta E_E \quad (2.28a)$$

$$= \frac{A}{2}K + \frac{B}{4} \frac{\frac{3}{2}K(K+1) - 2IJ(I+1)(J+1)}{IJ(2I-1)(2J-1)} \quad (2.28b)$$

With  $K$ ,  $A$  and  $B$  as previously described. So the absolute energy of each hyperfine level may be determined by:

$$E(IJF) = E_J + \frac{A}{2}K + \frac{B}{4} \frac{\frac{3}{2}K(K+1) - 2IJ(I+1)(J+1)}{IJ(2I-1)(2J-1)} \quad (2.29)$$

With  $E_J$  the energy of the corresponding fine structure level. We can then obtain all the hyperfine energies by running the quantum numbers  $F$ ,  $I$  and  $J$  whilst obeying the quantum selection rules in the  $E(IFJ)$  equation. Using this characterization of the hyperfine spectrum the data observed during laser spectroscopy experiments can be fitted and interpreted. The frequency spectra are used to extract not only the electric and magnetic nuclear moments but also the spin of the nucleus. The magnitude of

the splittings relate to the moments whilst the number of peaks relate to nuclear spin assignments.

### 2.2.2 Mean Square Charge Radius and Shape

The nuclear potential is what binds the neutrons and protons in the nucleus, it is a combination of both electromagnetic and strong forces. The form of the nuclear potential is unique to each nucleus and dependant on the quantities and energies of its constituents and its shape. It determines the overall characteristics of the nucleus. An initial property of the nucleus that is of great importance is the nuclear mass ( $m_n$ ):

$$m_n = \sum_i^n m_i - \frac{E_b}{c^2} \quad (2.30)$$

with  $m_i$  the mass of the  $i^{th}$  constituent of the nucleus and  $E_b$  the binding energy or mass defect. With this nuclear mass, which has been characterized for most of the nuclear chart, we can make first order estimates of nuclear density and its evolution across isotope chains. When adding or removing neutrons, changes in shape of the nucleus occur and configuration changes can be observed by measuring the nuclear size from isotope to isotope and looking for sudden non linear shifts. The issue with defining the radius of the atomic nucleus is that it does not possess definite boundaries. On the other hand the nucleus can be modelled as a sphere of positive charge. The radius of this sphere or charge radius allows a measure of the size of an atomic nucleus. It is defined as the radius over which the electrostatic charge of the protons are non negligible. The charge radius was first empirically estimated using scattering experiments and assuming the nucleus being a perfectly spherical object possessing uniform charge distribution. This approximation gives the following result for radius and mean square charge radius or MSCR [25]:

$$r = r_0 A^{1/3} \quad (2.31a)$$

$$\langle r^2 \rangle = \frac{3}{5} r_0^2 A^{2/3} \quad (2.31b)$$

With  $r_0 \approx 1.2$  fm and A the atomic mass number. However, nuclei are not solid spheres with finite bounds but are subject to vibrations and should be considered as objects with diffuse outer surface such as tennis balls. The spatial extent of the charge radius

is then defined by the second radial moment such that the mean square charge radius is [19]:

$$\langle r^2 \rangle = \frac{\int_0^\infty \rho(\vec{r}) r^2 d^3r}{\int_0^\infty \rho(\vec{r}) d^3r} \quad (2.32)$$

with  $\rho(\vec{r})$  the charge density of the nucleus. The denominator is the total charge of the nucleus  $Ze$ . As the charge density of the nucleus is related to the nuclear charge distribution then any deviation from sphericity will affect it such that the mean square charge radius can be written in such a way to account for deformation [19, 26] :

$$\langle r^2 \rangle = \langle r^2 \rangle_{sph} \left( 1 + \frac{5}{4\pi} \sum_{i=2}^{\infty} \langle \beta_i^2 \rangle \right) \quad (2.33a)$$

$$\approx \langle r^2 \rangle_{sph} \left( 1 + \frac{5}{4\pi} \langle \beta_2^2 \rangle \right) \quad (2.33b)$$

Where  $\langle r^2 \rangle_{sph}$  is the mean square radius assuming perfect sphericity and charge distribution from Eqn. 2.31 and  $\langle \beta_i^2 \rangle$  is the deformation parameter of order  $i$  of which generally only the first quadrupole order is kept. When studying an isotope chain, laser spectroscopy affords a very accurate measure on the changes in MSCR and so it is generally not the absolute mean square charge radius that is reported but the variation in MSCR from a reference isotope such that:

$$\delta \langle r^2 \rangle^{A,A'} = \langle r^2 \rangle^A - \langle r^2 \rangle^{A'} \quad (2.34)$$

With  $A$  the atomic number of the measured isotope and  $A'$  that of the generally more stable and easily produced reference. In practice  $\delta \langle r^2 \rangle^{A,A'}$  is extracted by calculating the field shift and using Eqn. 2.20 which does require some detailed theoretical calculations. This only has to be performed once per isotope chain due to the absence of any neutron-dependent term in the equation. Once the field shift and an empirical value for the specific mass shift have been obtained then the results can be combined in Eqn. 2.22. Inserting the experimentally measured isotope shift and subtracting the mass shift in Eq. 2.22 allow us to evaluate the field shift. The field shift can then be used to evaluate the change in MSCR  $\delta \langle r^2 \rangle^{A,A'}$ .

Changes in mean square quadrupole deformations  $\langle \beta_2^2 \rangle$  can be obtained from changes in mean square charge radii using the following relation [27]:

$$\delta \langle r^2 \rangle = \frac{5 \langle r^2 \rangle_{sph}}{4\pi} \delta \langle \beta_2^2 \rangle \quad (2.35)$$

The  $\beta_2$  deformation parameters can be used to understand single and collective trends in nuclear deformation. When disagreements occur between measured  $\langle\beta_2\rangle$  and  $\langle\beta_2^2\rangle$  they are associated to the dynamic component  $\beta_{dyn}^2$  of the deformation that would produce a MSCR larger than what would be expected from the static deformation alone. This relation can be expressed as:

$$\beta_{rms}^2 = \langle\beta_2\rangle^2 + (\langle\beta_2^2\rangle - \langle\beta_2\rangle^2) = \beta_{static}^2 + \beta_{dyn}^2 \quad (2.36)$$

Observing the change in the dynamic contribution of the nucleus deformation allows us to infer the collective nature of nuclear deformation. In particular an increase in the dynamic deformation can be described as a "softening" of the nuclear core, as the dynamic movement of the nucleus produces a larger time averaged charge radius. On the other hand a decrease in the dynamic component can be described as a "hardening" of the core towards a more rigid system where the deformation of the system can be attributed to its static shape.

When neutrons are added to a nuclear potential well, they occupy higher and higher orbitals and so the nuclear shape arrangement varies as a result. The change of MSCR across an isotope chain does not produce a precise measurements of the shape of the nucleus but it does afford a accurate measure of shape deformation. The change in MSCR along with the computations of the quadrupole moments will yield information on nuclear shape both statically and dynamically along the isotope chain. Deformation can be visualized by changes of the MSCR with respects to the predictions, assuming perfect sphericity. The analysis can be improved when data from several adjacent isotopes is available. The presence and evolution of deformation can be seen in the rate at which the MSCR changes. Sudden trend changes that appear as kinks in the MSCR plots along an isotope chain indicate that the shape of the nucleus is likely undergoing considerable change. In this way laser spectroscopy can afford insights into the evolution and onset of deformation of nuclei across isotope chains which can be compared to neighbouring element chains to extract larger trends useful to the nuclear chart.

## Chapter 3

# Experimental Methods of Collinear Fast Beam Spectroscopy

### 3.1 Radioactive Ion Production at TRIUMF

The TRIUMF facility located in Vancouver houses the largest cyclotron in the world. The 500 MeV cyclotron is fed by injecting negative hydrogen ions vertically and directly into its centre. The hydrogen ions are then circulated and accelerated around the cyclotron until they are stripped using a  $25\mu\text{m}$  thin carbon foil to produce proton beams. This extraction method allows simultaneous extraction of multiple proton beams at different locations and energies which allows the facility to undertake multiple endeavours for fundamental research, industrial application and medical treatments simultaneously.

One of the proton beam users is the Isotope Separator and ACcelerator or ISAC facility which often employs a 500 MeV proton beam at around  $100\ \mu\text{A}$  to bombard targets such as thick uranium carbide kept at  $2000^\circ\text{C}$  for the rubidium or Rb work undertaken in Chapter 3. The reaction products leave the target foil and diffuse into transfer tubes coupled to the ion source. Once the products are ionized they are extracted and sent to a two stage high resolution mass separator (resolving power  $\frac{m}{\delta m} \approx 2500$ ). The ion beam of interest is then tuned along the beam-lines into the ISAC experimental area. Using this method the ISAC facility is capable of producing and providing experiments with a wide array of mass-separated rare isotopes which is ideal for the CFBS experiment

as it overcomes the difficulties associated to the production, confinement and short lifetimes of these rare radioactive isotopes. The production yield of each element and its corresponding isotopes depends heavily on the target ion source combination.

## 3.2 The CFBS Beamline

Within the ISAC facility hall, rare and radioactive ion beams are delivered to the CFBS beamline as is shown in Figure 3.1. The setup contains several steering electrodes to fine tune the ion beam and several MCPs (MultiChannel Plate detectors) which generate electrical signal when struck by ions to check the beam transmission and efficiency. The MCPs can be removed once calibrations are taken in this segment to allow unobscured ion flight to the next stage. Equally an off beamline axis RFQ (Radio Frequency Quadrupole) is shared with the TITAN (TRIUMF's Ion Trap for Atomic and Nuclear Science) collaboration. The ions can then either be sent to the RFQ which is used to bunch the ion beam so that the laser spectroscopy experiment can be carried out on bunched ion beams or directly to the laser spectroscopy beamline via the RFQ bypass in order to carry out spectroscopy on a continuous ion beam. The advantages and workings on the RFQ are discussed in more detail in section 3.2.2.

### 3.2.1 Collinear Laser Spectroscopy

Historically laser spectroscopy has been undertaken by crossing a single mode laser beam with atoms created in an oven through evaporation. This crossed beam technique has since given way to CFBS as laser spectroscopy strived to observe and study rare and short lived radioactive nuclides. These can only be produced at radioactive ion beam facilities such as TRIUMF. In order to make optimal use of rare and low yield elements produced at such facilities, obtaining the best overlap of ion beam and laser beam is of utmost importance. The accelerated ion or atom beam of interest is collinearly overlapped with single mode, narrow line-width, continuous wave lasers [28]. One of the main issues with studying gaseous samples produced by evaporation was the velocity spread of its constituents due to thermal motion. This velocity spread leads to the Doppler effect due to the approaching and receding particle velocities with respects to the light source [29]. The observer then observes a Doppler broadened spectral line-width. The

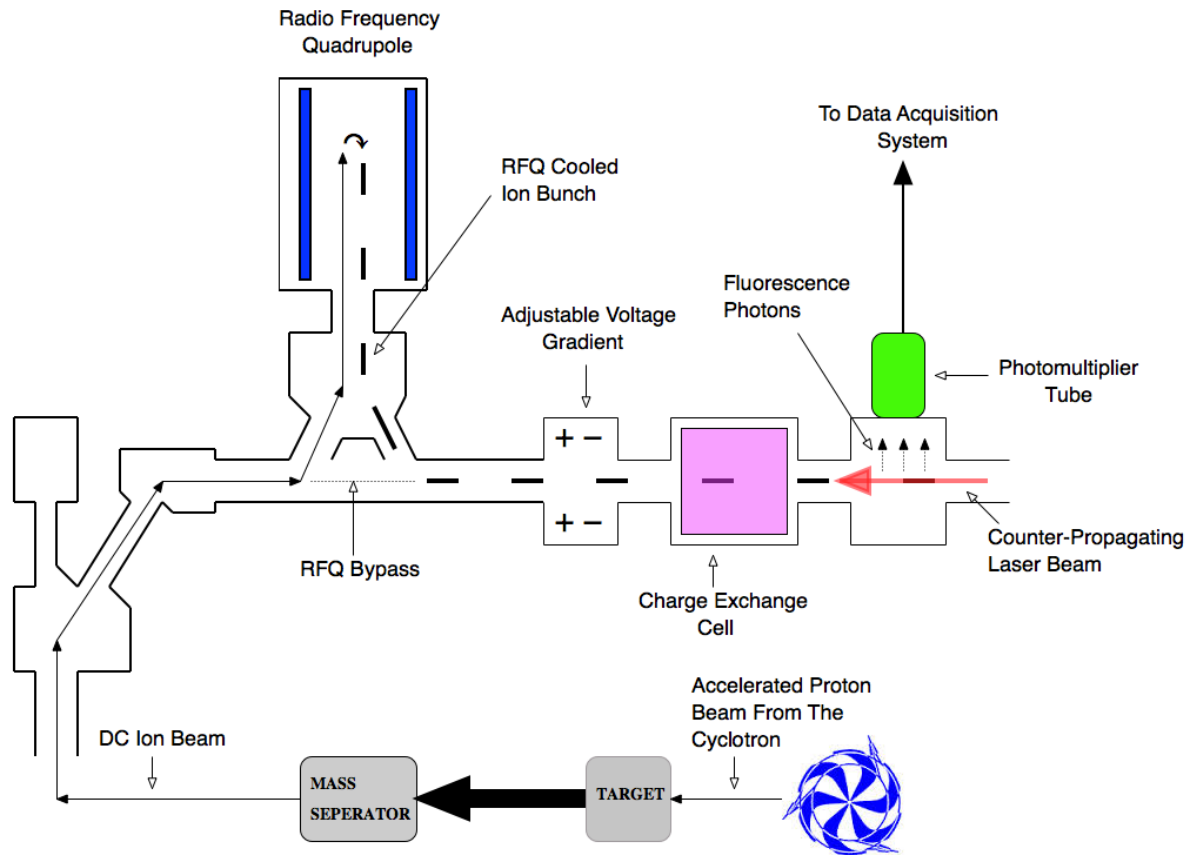


FIGURE 3.1: Overview of the CFBS experiment beamline

beam's acceleration reduces its Doppler line-width as  $\Delta v = \frac{\Delta E}{mv}$ . With  $\Delta v$ , the velocity spread of the beam, which is greatly reduced in accelerated beams compared to in diffuse products of evaporation. The production of ions by bombardment produces a wide spread of ion velocities, it is therefore essential to accelerate the beam to greatly reduce velocity spread and so obtain Doppler line-widths small enough to investigate hyperfine structures using CFBS.

Figure 3.1 schematically shows the CFBS experiments beamline. The cyclotron at TRIUMF is used to accelerate the protons used to bombard targets to produce the rare isotopes which are then sent to the CFBS experiment. These isotopes, after undergoing mass separation in order to select the isotope of interest are either directly sent to the CFBS beamline or via the ion bunching RFQ. The ions are then tuned into resonance with the incoming laser beam using an adjustable voltage gradient to create an

accelerating Coulomb potential for the ions. The ions are then neutralized in a charge exchange cell and finally interact with the collinearly propagating laser light in the Light Interaction Region (LIR) where any fluorescence photons are collected off axis by a photomultiplier tube. The lifetime of the transitions are of the order 20-30 ns. The CFBS experiment at TRIUMF scans the post acceleration voltage instead of the laser frequency as done by early laser spectroscopy experiments as this affords greater stability and reproducibility [18]. The scanning voltage is applied just before the charge exchange cell which is itself positioned just before LIR. This allows the atoms of interest to be shifted into resonance with the collinearly overlapped laser beam whilst keeping the laser frequency locked to a reference frequency stabilized HeNe. This technique, called Doppler tuning, minimizes the systematic effects associated to scanning laser frequencies.

### 3.2.2 Radio Frequency Quadrupole and Light Interaction Region

RFQ coolers and bunchers have been used at radioactive beam facilities to prepare ion beams for experimental analysis for many years [30]. They are often linear Paul traps built on axis to the ion beam in order to accumulate, cool and bunch the ions. The RFQ is shared with the TITAN collaboration and so is located off axis to the CFBS beamline in order to facilitate use by both experimental beam-lines. Therefore the ion beam has to be tuned into the RFQ and out to the CFBS beamline using deflection electrodes.

The RFQ consists of a segmented quadrupole ion trap combining RF electric oscillations, providing radial confinement. It equally possess a set of differentially applied DC voltages which provide axial ion trapping. The RFQ is floated at a voltage just a few volts below the ion source's bias to allow the beam to decelerate inside to the RFQ. The ions are accumulated using this capture potential for a certain accumulation time which depends on the lifetime of the said radioactive ion. These periods are generally around 30-250ms for CFBS spectroscopy. Inside the RFQ, the ions are collisionally cooled with an inert high purity buffer gas consisting of helium at  $10^{-2}$  torr which leads to a loss of residual energy until a thermal equilibrium with the room temperature buffer gas is achieved. Velocity spreads  $\Delta v_0$  prior to entering the RFQ are cooled according to the following equation:

$$\Delta v \approx \frac{1}{2} \left( \frac{k_B T}{eV} \right)^{1/2} \Delta v_0 \quad (3.1)$$

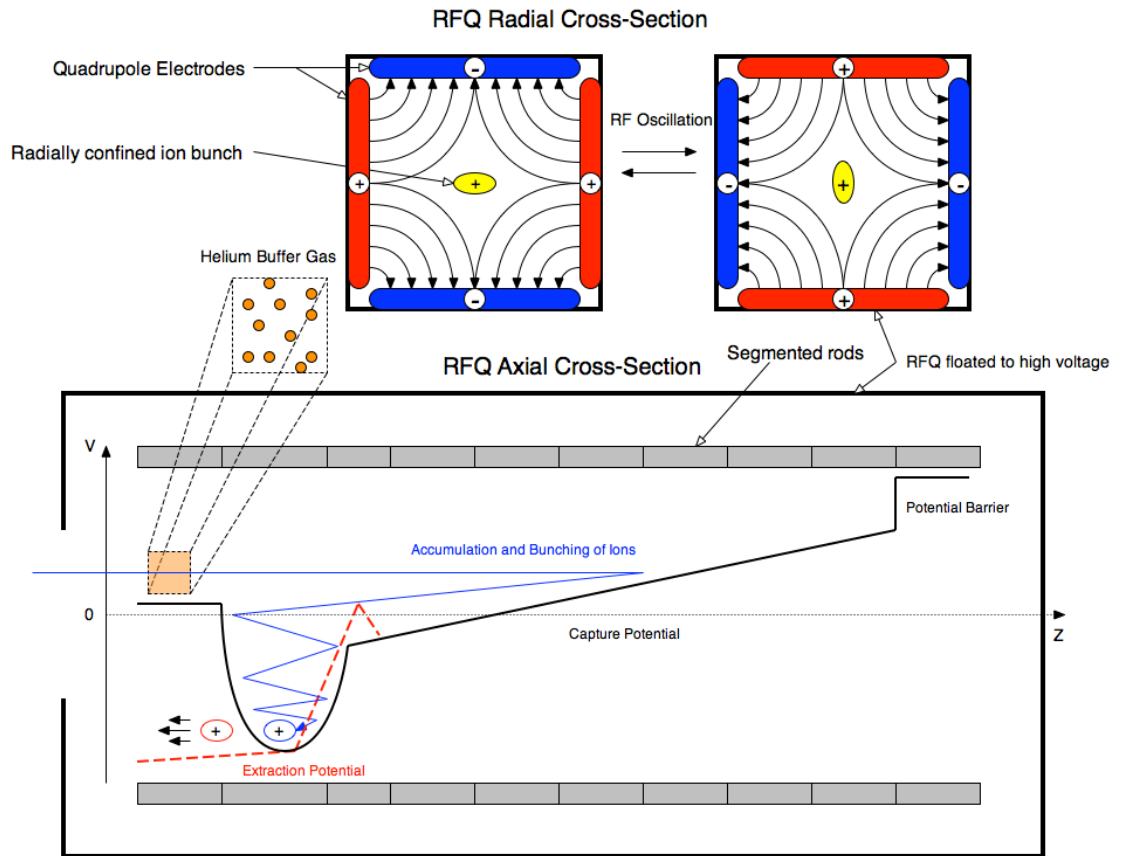


FIGURE 3.2: RFQ Overview: Radial electric fields (top) and axial trapping potential (bottom)

with  $k_B T$  the energy spread whilst exiting the RFQ.

The RFQ is composed of four rods arranged around the trapping region to which square wave, RF quadrupole fields are applied with adjacent rods having opposite phase. These fields induce a centering force that confine the ions to the middle of the RFQ, confining them radially as seen in the top section of Figure 3.2. The rods are sectioned longitudinally into segments which allow for an electrostatic potential gradient to be applied along the beam axis. The segmentation grants the possibility to stop the ions in the RFQ and smoothly bring the cooled bunches to the front of the RFQ for extraction using a variable potential well as illustrated in the bottom section of Figure 3.2. A repulsive capture potential is applied to the first segment to provide a barrier and prevent ions leaving the RFQ. In this way the ions are confined in 3 dimensions. The size and release

of the bunch can be controlled using accumulation times and variable potentials along the segmented sections of the RFQ. Typical bunches have  $10^4 - 10^5$  ions per bunch [31]. Typical settings for the RFQ are accumulation times of around 100 ms and an extraction window of around 100  $\mu$ s. The extraction of the bunches is then started by changing the repulsive potential on the first section of rods to an attractive one and putting a repulsive barrier behind the accumulated bunch to "kick" out the ion bunch. The bunched nature of the beam is doubly advantageous to our experiment. Firstly as the ions are confined to a smaller region in space and energy they will be easier to observe and excite due to their higher density. The bunches have smaller energy spreads and so their time of flight (TOF) to the PhotoMultiplier Tubes (PMT), where we acquire our data can be calibrated. The release of the ion bunch by the RFQ can be used as a trigger and coupled with the known time of flight allows us to gate our data acquisition and increase our signal to noise ratio. Using the RFQ to cool and bunch our ion beam allows us to reduce our background by 4 to 5 orders of magnitude [26] with respect to measurements using continuous ion beams.

In order to perform laser spectroscopy on neutral atoms it is necessary to neutralize the nuclide of interest, in particular rubidium isotopes in our case. The nuclides that are steered to the RFQ to be bunched and cooled as previously described need to be charged ions in order to be affected by the steering electrodes of the beam-lines and the trapping potential of the RFQ. The ions are neutralized in a charge exchange cell located just before the Light Interaction Region (LIR) when they no longer need steering or accelerating elements. The incoming ions are held just off resonance with the collinearly overlapped laser beam in order to avoid optically pumping the ions' cycling transition. Just before the LIR and charge exchange cell, accelerating electrodes use a voltage gradient to bring the incoming bunched ions from the RFQ into resonance with the laser frequency. They are then neutralized in the charge exchange cell using an inert alkali vapour such as rubidium or sodium depending on the properties of the ions of interest. When the heated alkali vapour and the incoming ion bunches collide valence electrons are stripped from the alkali and neutralize the ions. To ensure adequate neutralization it is important to make sure that the kinetic energy of the collisions is equivalent to the ionization energy of the valence electrons of the chosen alkali vapour. Equally important is the neutralization efficiency which for our experiments hovers around 0.5; this can be altered by changing the temperature of the vapour cell. This means that only half of the

incoming ions are neutralized and so are observable with the laser. This neutralization efficiency can be improved but doing so would introduce undesired energy broadening, due to Brownian motion of the neutralization vapour to the ion bunch and would diminish the amount of nuclides which are Doppler shifted into resonance with the laser. This would diminish resolution on the measurement. Once the ion bunch from the RFQ has been Doppler tuned using the accelerating electrodes and neutralized in the charge exchange cell it starts the electronic excitation de-excitation cycle which produces fluorescence photons as described in Chapter 1. These photons are emitted isotropically within the LIR where a spherical mirror focuses them onto a PMT to increase the solid angle of photon acquisition and improve statistics. It is these fluorescent photons that constitute our hyperfine frequency spectra as shown in Chapter 2.

### 3.2.3 The Laser System

The laser system is housed in a temperature controlled environment which eliminates large fluctuation in laser and etalon cavity sizes. Thermal expansion of cavity materials results in significant loss of stability in the lasers' power and frequency. The room is equally kept at higher than atmospheric pressure and contains many filtering units to prevent the excessive introduction of dust and particulates to the system that might damage it. The laser system and associated optics is seated on an optical table to reduce vibrational noise and clamp optical elements.

The laser system consists of a frequency stabilized Coherent Monolithic Block Resonator (MBR) which is a Titanium:Sapphire laser using a titanium doped sapphire as the gain medium. The MBR is itself pumped using an argon ion laser with a wavelength mixture of 488 nm and 514 nm which is introduced collinearly into the MBR laser resonator. The MBR is operated at 780 nm to drive the  $D_2$  transition ( $5s^2S_{\frac{1}{2}}(0.00\text{cm}^{-1}) \mapsto 5p^2P_{\frac{3}{2}}(12816.56\text{cm}^{-1})$ ) in rubidium. The polarization of the MBR is imposed using a Faraday rotator, optical elements at Brewster's angle and a manually tuneable birefringent filter. Single mode lasing and finer frequency selection is achieved using the ultra-thin intra-cavity etalon to counter mode hopping brought about by mechanical vibrations. The etalon is controlled by a galvanometer with mounted Brewster plates and a piezo crystal. Together they allow for a mode-hop-free continuous scanning of up to 30 GHz and ultra-narrow line-width operation (less than 100kHz) with

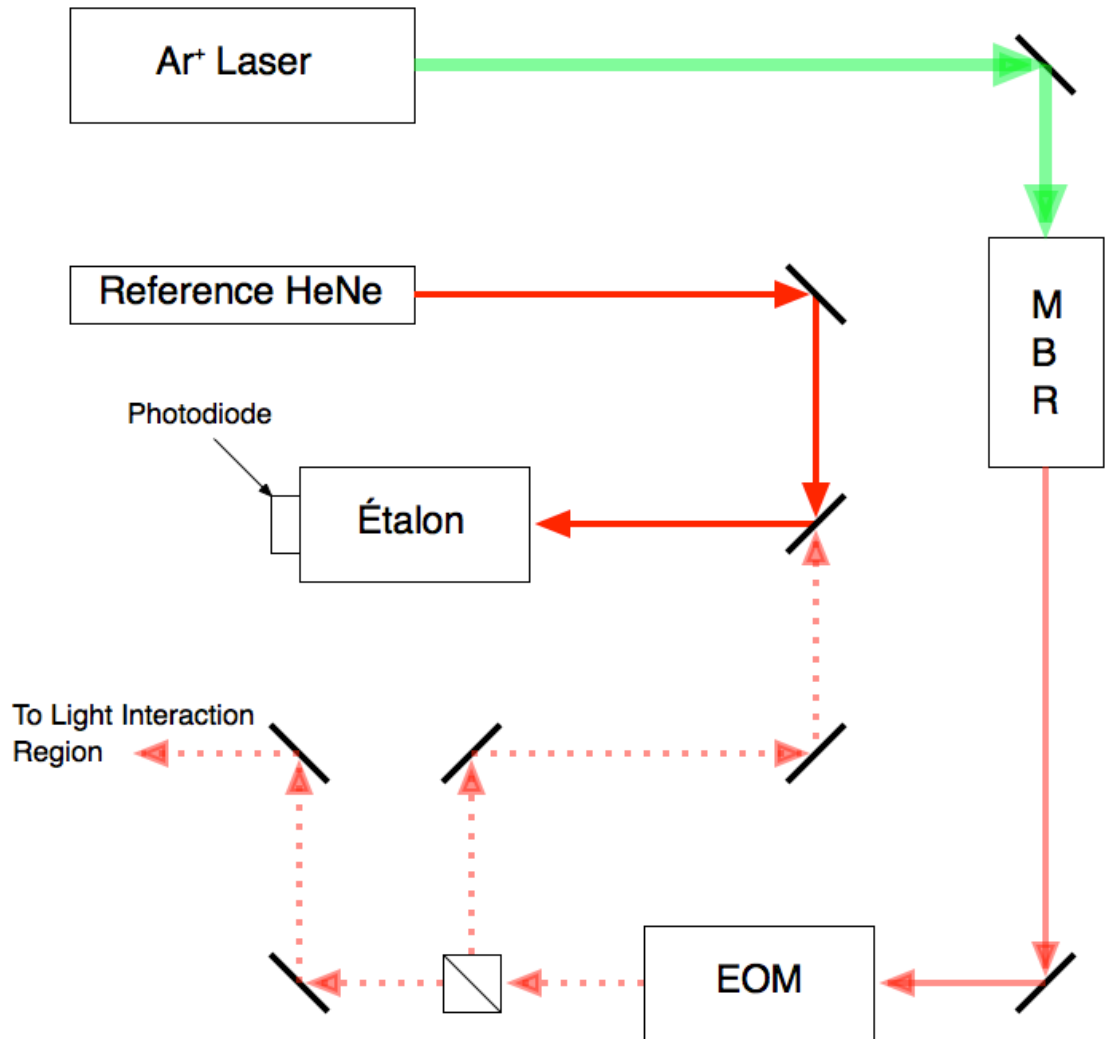


FIGURE 3.3: Diagram of the Laser System for CFBS

fast feedback. Long term frequency stabilization and control of the MBR frequency are essential to the running of this experiment as they are the tools that give us the precision on the hyperfine structure we are investigating. The laser lock is achieved using a scanning confocal Fabry-Perot etalon (CFP) and a HeNe reference laser as shown in Figure 3.3. The precision of the MBR laser lock provides the narrow resolution required for the hyperfine measurements undertaken by CFBS. The implementation of a new laser locking program and more details about the methods and tools employed to achieve the laser lock are discussed in depth in Chapter 5 and was subject of a large portion of this

Masters research project. The frequency lock of the excitation laser is a major source of error in hyperfine measurements. By both characterizing and improving the frequency stabilization, the results of CFBS group can be improved.

The MBR light is then sent to the beamline and LIR using an optical fibre. Before being sent down the beamline a set of wave-plates and polarizing beam splitting cubes are employed to ensure linear polarization and control laser power. In order to align the laser beam a set of 3mm retractable in-beamline apertures are employed. The transmitted laser power is then measured using a power-meter located at the exit of the beamline at the laser beam dump. The same apertures are used for ion bunches with diagnostics given by retractable micro-channel plates located before and after the LIR. This allows us to overlap the laser and ion bunches during calibration runs. Equally a beam-profiling camera is employed to optimize the optical telescope used to focus the laser light at the LIR. The camera is off axis but the same distance from the LIR, so focusing at this camera is equivalent to focusing at the LIR. The diameter of the beam-spot can equally be determined and compared to that of the ion bunches to insure optimal overlap.

### 3.2.4 Laser Chopping with an EOM

A limiting factor on the CFBS method used to obtain hyperfine structure spectra is the hyperfine pumping between cycling and non cycling transitions in the level scheme. Cycling transitions are a result of quantum selection rules, as we are using electric dipoles (photons) to excite our hyperfine transitions. In this way the only transitions allowed obey:

$$\Delta F = 0 \text{ or } \pm 1 \quad (3.2)$$

except  $F_{initial} = 0 \rightarrow F_{final} = 0$  transitions which are forbidden. This arises from the vector equation :  $\vec{F} = \vec{I} + \vec{J}$  and so if the initial and final F projection terms are zero then there is no possible transition that satisfies this vector equation. To add to these selection rules the hyperfine coupling matrix favours high angular momentum transitions [32]. An example of these selection rules and the cycling transition that arises from it can be seen in the following Figure 3.4 for the  $D_2$  transition in  $^{87}\text{Rb}$ [33]:

For the  $D_2$  transitions in  $^{87}\text{Rb}$  electrons from the  $S_{\frac{1}{2}}$  hyperfine levels have three upward transition possibilities depending on its original ground level. In this example

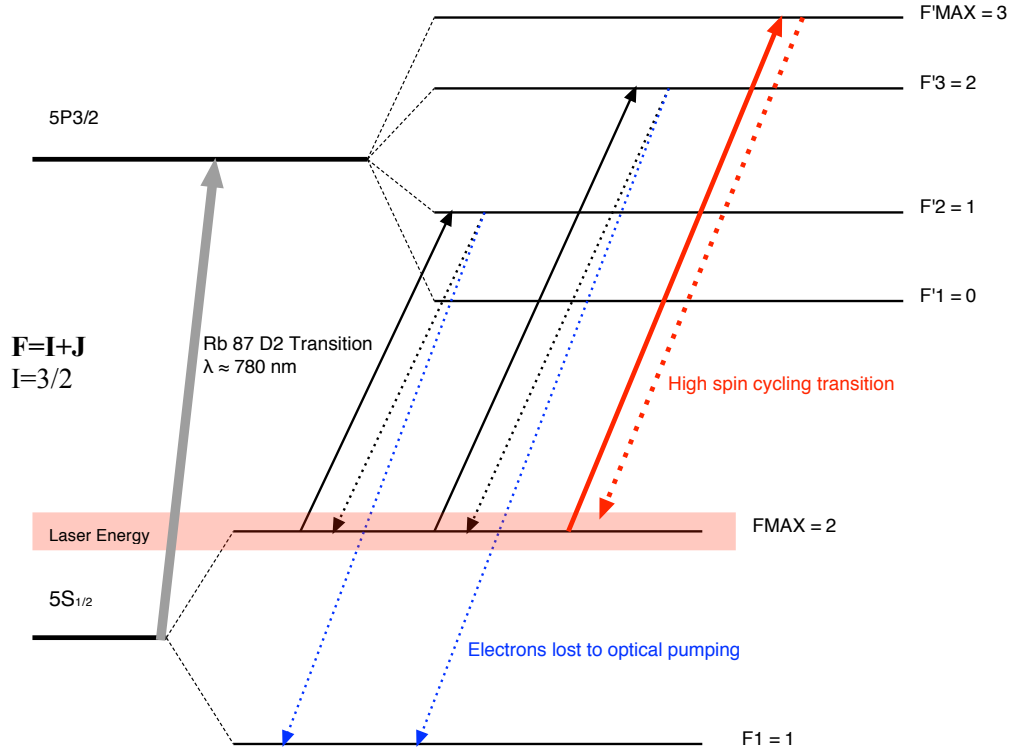


FIGURE 3.4: Illustration of the cycling transition and optical pumping

using the  $F=2$  ground state which can be excited to the  $F'_{max}$  hyperfine levels. Once excited electrons can only return to the  $S_{\frac{1}{2}}$  level via the spin cycling transitions whilst the other hyperfine levels can decay to the two  $F$ -ground levels. Due to the nature of the narrow frequency width with which we are scanning the laser, we only excited one of the  $F$ -ground state levels in such a way that electrons that are excited via processes other than the cycling transition have the possibility to de-excite to another  $F$ -ground state than the one it originated from. Those electrons are therefore no longer excitable by our laser and so no longer contribute to the frequency spectrum. When the laser is used in continuous wave mode (CW) multiple excitation de-excitation cycles leads to pumping of the  $F$ -ground state as electrons will not return to the  $F$ -ground state our laser frequency is scanning. In this way the relative intensity of the cycling transition peaks will grow with respect to the non cycling transitions as the number of cycles increases. The magnitude of this effect can be understood as explained in [34]. In order to get an idea of the peak suppression factor, it has been calculated that for a single atom that after two successive scatterings the secondary peaks are roughly halved whilst after 5 all other peaks other than the cycling transition are effectively suppressed.

In order to extract meaningful hyperfine spectra the laser power can be lowered to diminish this effect, but as laser power is lowered the time required to obtain enough photon counts to build a statistically significant and fit-able spectrum increases. The signal-to-noise ratio is equally negatively affected by a reduction in laser power. In order to circumvent these issues the use of an Electro-Optical Modulator (EOM) crystal was implemented at the CFBS experiment. The EOM allows us to "chop" the laser beam and obtain bursts of laser light whose duration can be controlled and set to the order of the hyperfine lifetime  $\tau$ . The EOM, which is placed on the laser path is controlled by a signal generator which allows modulation of the laser beam by using a reference square wave to trigger the switches between stopping and allowing the laser light to pass to the LIR. By calibrating the waveform generator's frequency each nuclide bunch will only see one burst of light for a time of the order of  $\tau$  ( $\approx 12\text{ns}$ ) between the moment it is neutralized and the moment it passes the LIR. This limits the hyperfine transition cycles to around one and eliminates the hyperfine pumping whilst preserving the peak intensity ratios. An added advantage of this technique is that we can employ higher laser energies than in the classic CW set up as the average power the atom bunch receives is still low due to the short time burst.

### 3.3 Data Acquisition

#### 3.3.1 Shape and Width of Spectral Lines

Even though the theory in Chapter 2 predicted discrete hyperfine lines in atoms they nevertheless possess a finite energy spread which is a result of the Heisenberg uncertainty principle in such a way that the line-width  $\Delta\nu_i$  of an excited atomic state with finite energy  $\Delta E_i$  for a transition of frequency  $\nu_i$  to the ground state with hyperfine lifetime  $\tau_i$  can be written as:

$$\Delta\nu_i = \frac{\Delta E_i}{h} = \frac{1}{2\pi\tau_i} = \Gamma_{natural} \quad (3.3)$$

With  $\Gamma_{natural}$  the natural line-width of a transition and  $h$  Planck's constant. For example the natural line-width of  $^{87}\text{Rb}$  hyperfine structures is of 6MHz as their listed hyperfine lifetime  $\tau$  is of approximately 26.3 ns [35]. The natural line-width is the Full Width Half

Maximum (FWHM) of a Lorentzian profile in measured intensity:

$$I(\nu) = I_0 \frac{\Gamma_{natural}}{(\nu_0 - \nu)^2 + \Gamma_{natural}^2} \quad (3.4)$$

with  $I_0$  the normalization constant. Equally contributing to the energy spread of hyperfine lines is the thermal energy fluctuations in atom bunches. They follow a Maxwell-Boltzman distribution and contribute to a Doppler broadening of the spectral lines. The velocity spread of the atom bunch can be written as:

$$I(\nu) = I_0 e^{-\frac{mv^2}{2k_b T}} \quad (3.5)$$

It is a Gaussian profile related to the root mean squared velocity  $v = \sqrt{2k_b T/m}$  of the atom bunch. In this way particles with a net non-zero velocity moving towards or away from the laser beam will have slightly shifted centroids which leads to a wider spectral line. The cooling of the beam in the RFQ helps diminish this effect but cannot fully remove it. Therefore the FWHM for this profile is [36]:

$$\gamma = \nu_i \sqrt{\frac{8k_b T \ln 2}{mc^2}} \quad (3.6)$$

With  $\nu_i$  is the transition frequency and  $k_b T$  the thermal energy of the atom bunch.

In order to account for these two effects when finding a line profile to fit our hyperfine peaks we use a Voigt profile. The Lorentzian profile  $L$  of the atomic spectral lines due to the Uncertainty principle is convoluted with the Gaussian profile  $G$  arising from the thermal Doppler broadening. The new line-shape is therefore [36]:

$$I(\nu, \Gamma, \gamma) = \int_0^\infty G(\nu, \gamma) L(\nu, \Gamma) d\nu \quad (3.7)$$

As this profile cannot be evaluated analytically it must be numerically evaluated during the fitting process. A term of particular interest that uniquely describes the shape of the Voigt profile is called the Lorentzian fraction ( $\gamma/\Gamma$ ) which is the ratio of the FWHMs of the Gaussian and Lorentzian profiles

Another important factor to take into account when analyzing hyperfine lines is the

Doppler shift that arises from the last electrostatic acceleration of the ion bunch before the vapour neutralization cell. This Doppler shift does not affect the hyperfine line-width, it is actually used to bring an ion bunch into resonance with the collinearly propagating laser beam. The shift moves the ion bunch to the required velocity to probe the hyperfine levels. For a ion bunch travelling at velocity  $\beta = \frac{v}{c}$  with centroid frequency  $\nu$  the Doppler shift can be expressed as :

$$\nu = \nu_{laser} \sqrt{\frac{1 + \beta}{1 - \beta}} \quad (3.8)$$

With  $\nu_{laser}$  the laser frequency and  $\beta$  the relativistic parameter such that:

$$\beta = \sqrt{2 \frac{E_{bunch}}{E_{r-mass}}} \quad (3.9)$$

With  $E_{bunch}$  the total kinetic energy of the bunch and  $E_{r-mass} = mc^2$  the rest mass.

Finally PMT counts corresponding to photon detections obey Poisson count statistics in such a way that the uncertainty associated to PMT counts  $C$  will be of:

$$\delta C = \sqrt{C} \quad (3.10)$$

This is used when doing error analysis for this work. Each point on the hyperfine spectrum will have an error of the square root of the photon counts that constitute that point. Most of the noise in the measurements arises from the scatter of laser light inside the beamline. This is why a good laser alignment in the beamline is required to reduce background.

### 3.3.2 Isotope Shift Measurements

As described in Chapter 2, in order to measure the isotope shift a reference isotope is needed. This is to account for the systematic errors that arise from the beam delivery energy which is often subject to variations of the order of a couple of volts. For example for our rubidium experiment, the atomic mass 92 was used as a reference. A change in beam energy of a couple of volts within the typical 20keV beams gives rise to a frequency-space error conversion of approximately 6MHz per volt.

Given that isotope shifts are generally of the order of several hundred MHz a beam energy drift of a couple of volts introduces systematic errors to the measured isotope shift of the order of one percent. In order to account for this systematic error sequential measurements of hyperfine structures of a known calibration or reference isotope are taken. These calibration isotopes are generally easily produced with high yield to make their measurements fast and reliable due to their high statistics. Once a calibration hyperfine transition has been made, the hyperfine spectroscopy on the transition of interest on the rarer isotope can be undertaken. During post experimental data analysis the baseline shift in energy can be detected by comparing the hyperfine transition of the calibration isotope to its accepted value. The baseline shift can then be accounted for and corrected for the isotope of interest.

### 3.3.3 An MCS DAQ system

The Data Acquisition (DAQ) at the CFBS experiment has evolved from a previous iteration employing hardware triggers to use a continuously running software acquisition system called the MCS which is based with a continually running  $T=20$  ns clock which triggers data acquisition. The voltage on the final acceleration electrodes which Doppler tunes the incoming bunches into resonance with the laser beam is software controlled. A digital voltmeter (DVM) is coupled with a 16 bit DAC which produce a  $\pm 10V$  high precision control voltage. This control voltage is then fed into a KEPCO  $\times 100$  amplifier which has a  $\pm 1000V$  range whilst having the capacity to cross 0 V. In order to increase the energy levels we can probe with sufficient precision the KEPCO voltage is then added in series to a floating static adjustable ground with 0 to 5000V range power supply ( $V_0$ ) which is then finally fed to the acceleration electrodes such that the voltage on the electrodes  $V_{acc}$  can be written as:

$$V_{acc} = V_0 + A_{100}(V_{DAC} + n\Delta V_{step}) \quad (3.11)$$

With  $A_{100}$  the KEPCO amplification factor of 100.  $V_{DAC}$  is the DVM supplied control voltage set point and  $\Delta V_{step}$  the step size with  $n$  the step count used to scan the voltage. In order to obtain a voltage read-back for the DAQ system value for  $V_{acc}$ , a 10000:1 voltage divider is employed. When this system is set up in this fashion it gives a dynamic range of 2000V or close to 24GHz in equivalent frequency space. Figure 3.5

shows a schematic overview of the DAQ system.

A system of triggers and Pulse Programmable Gates (PPG) is employed to opti-

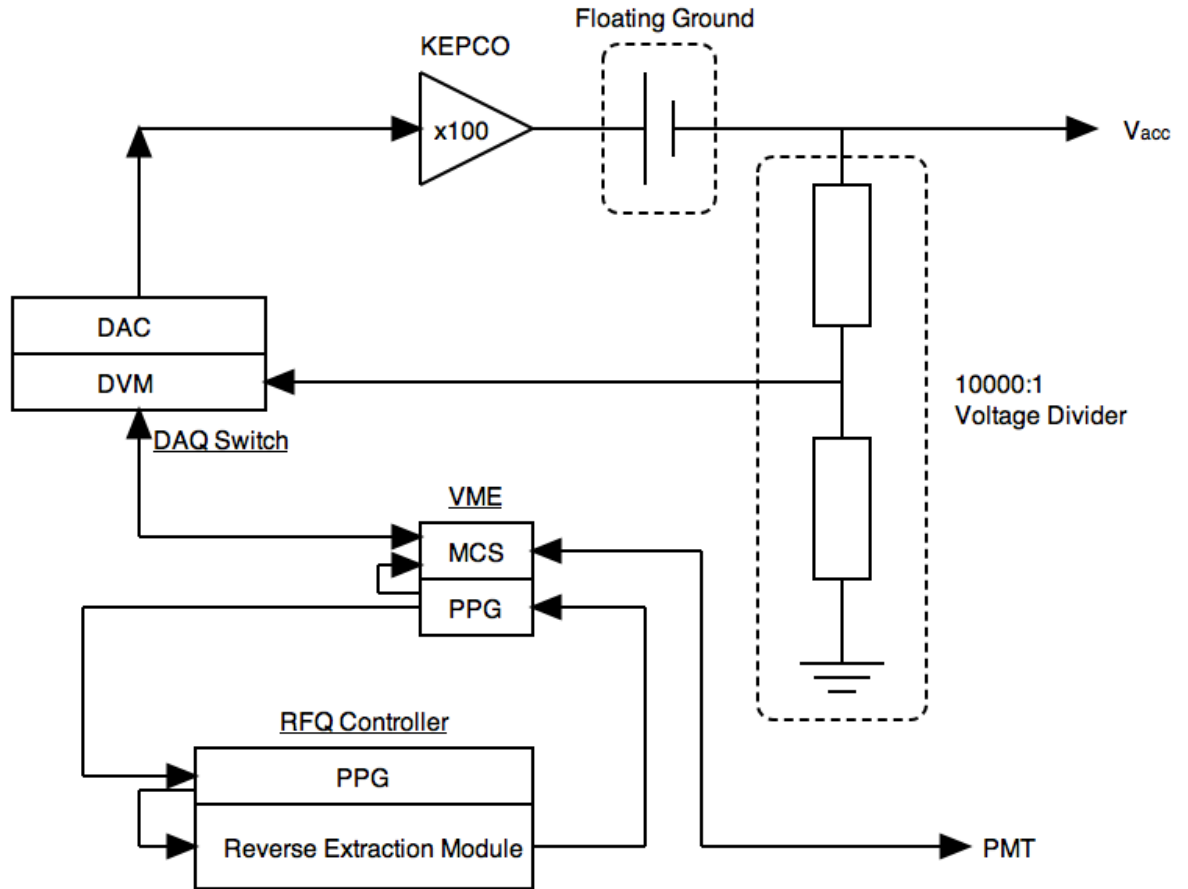


FIGURE 3.5: Diagram of the Data Acquisition (DAQ) and experiment control system. With DAC the digital to analog converter, MCS the multi-channel scalar and DVM the Digital voltmeter and PPG pulsed programmable gate.

mize data collection and reduce noise. A data acquisition and voltage scan cycle starts with the accumulation of ions in the RFQ. After an adjustable extraction/accumulation delay in which the ions are trapped and cooled inside the RFQ, the trapping potential is switched to an extraction potential with a kicker voltage which sends the ion bunch down the beamline. When the trapping potential is switched to an extraction potential a trigger is sent to the DAQ which starts the data acquisition and defines  $T=0$  in the DAQ read-back. The DAQ contains two independent MCS channels, one used to bin PMT counts in time-bins down to  $0.25\mu s$  and the other to perform diagnostic measurements on the collected data. PMT counts are only accepted in coincidence with the user

defined MCS gate generally set to a time superior to the time of flight (TOF) of the ion bunch from the RFQ to the PMT in order to not lose any statistics but still limit background noise. Figure 3.6 shows a whole PPG cycle for the MCS-DAQ system. The PPG cycle starts when the ions, after being cooled and bunched in the RFQ are ejected into the CFBS beamline. It ends after a user defined time delay to ensure resonance photons are measured on the PMT. For the rubidium work described in Chapter 4 the observation time was set to around  $200 \mu s$ , about twice the TOF. So using 100 time-bins at 50% MCS duty cycle with  $2 \mu s$  per time-bin results in around 400 PMT snapshots per PPG cycle. The PMT acquisition rate is determined by the dwell time (bin width of  $\sim 2 \mu s$ ) and the MCS bin count ( $\sim 100$ ). After a certain user-defined number of PPG cycles the electrode voltage is incremented by a pre-set step to enable sweeps across hyperfine structures and the whole cycle begins anew. This system allows for a fully time independent view of the ion bunch profile and hyperfine structure. It equally allows for real time troubleshooting of RFQ settings. This system therefore reduces background by up to four orders of magnitude [37] with respect to hardware gating DAQ techniques.

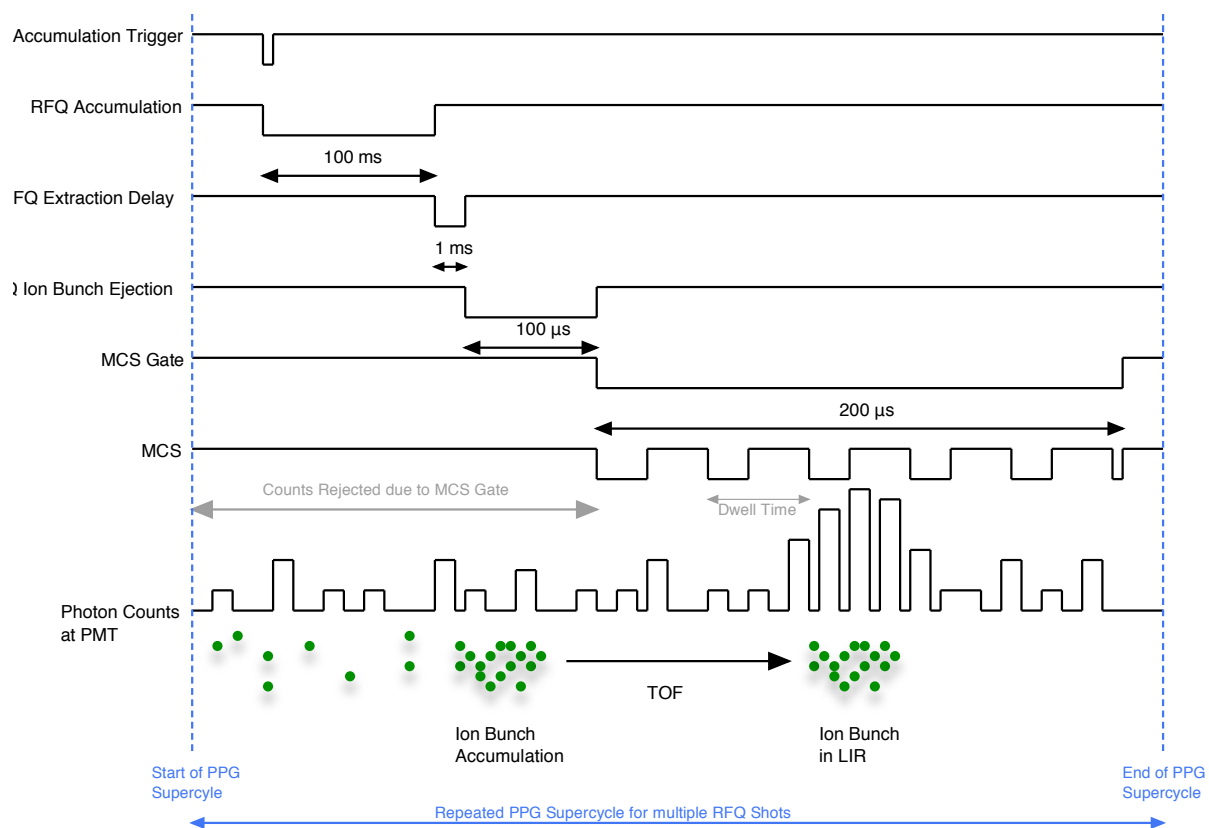


FIGURE 3.6: Triggering and Pulse Sequence for the MCS-DAQ system.

## Chapter 4

# Laser Spectroscopy on Neutron Rich Rubidium

Collinear Fast Beam Laser Spectroscopy experiments on the rubidium isotope chain have been performed over multiple experimental runs at the ISAC facility at TRIUMF since 2010. The author, having contributed to two rubidium experimental runs at TRIUMF, presents the motivation for these experiments and insights offered from their results on the nuclear structure of the neutron rich rubidium chain.

### 4.1 Physical Properties

Rubidium is an alkali metal with atomic number  $Z=37$ , discovered in 1861 by Bunsen and Kirchhoff [38] using an early form of spectroscopy: flame spectroscopy. It is only the second element after caesium to be discovered using spectroscopy and has distinctive bright red lines in its emission spectrum. Elemental rubidium, as other alkali metals, is extremely reactive and in particular has a very rapid oxidation in air. Because of this care must be taken to shield it from the atmosphere [39]. Rubidium metal being easily vaporized and having an accessible spectral absorption range made it an ideal candidate for early laser spectroscopy.

Since its discovery, probing of rubidium via laser spectroscopy has confirmed the existence of 31 isotopes ranging from  $^{71}\text{Rb}$  to  $^{102}\text{Rb}$  [40, 41]. Naturally occurring rubidium is a mix of two isotopes: the only stable rubidium isotope  $^{85}\text{Rb}$ , constituting 72.2%, and

the extremely long lived ( $\tau_{\frac{1}{2}} = 48.8 \times 10^9$  years)  $^{87}\text{Rb}$  which constitutes the other 27.8% of the natural rubidium [42]. Rubidium isotopes span across the  $N=50$  neutron shell closure with  $^{87}\text{Rb}$  possessing the  $N=50$  magic number [43] which explains its extremely long half life.

## 4.2 Extension of previous studies of the rubidium isotope chain

### 4.2.1 Previous work and motivations

The rubidium isotope chain has been the subject of extensive investigation using laser spectroscopy. Much of the spectroscopic work undertaken on this element was carried out by Thibault et al. in 1980 at the ISOLDE facility at CERN [41]. Thibault et al. used hyperfine laser spectroscopy to identify 23 isotopes and 6 long lived isomers ranging from  $^{76}\text{Rb}$  to  $^{98}\text{Rb}$ . Thibault et al measured various nuclear parameters such as nuclear spins, A and B coefficients and isotope shifts. From these measured quantities they deduced magnetic moments, quadrupole moments and changes in mean square charge radii. These results are presented in Tables 4.1 and 4.2 along with more recent results. Their comprehensive survey remains to this day an authority when it comes to hyperfine properties of the rubidium isotope chain.

Shape coexistence is a topic of much experimental and theoretical work in nuclear physics as it offers insight into the relation between single particle and collective modes of excitation in nuclear matter. A region of the nuclear chart that exhibits important and rapid quadrupole deformation is located about the  $N=60$  neutron sub shell closure. This has led the neutron rich  $A=100$  region to become very interesting to study in the context of nuclear deformation and shape coexistence. The rubidium isotope chain possessing  $Z=37$ , spans this region and presents an ideal candidate for further studies in shape coexistence using laser spectroscopy due to its sensitivity to changes in MSCR. The important deformation at  $N=60$  has been investigated using laser spectroscopy on rubidium isotopes by analyzing the evolution of MSCR across the chain initially by Thibault et al but more recently by the CFBS group at TRIUMF in the past couple of years. This characteristic deformation is also observed in the closest neighbouring

elements to rubidium:  $Z=36$  krypton (Kr) [44],  $Z=38$  strontium (Sr) [45] and  $Z=39$  yttrium (Yt)[46, 47]. All these elements show the characteristic sharp kink in change in MSCR around  $N=60$  as shown in Figure 4.1.

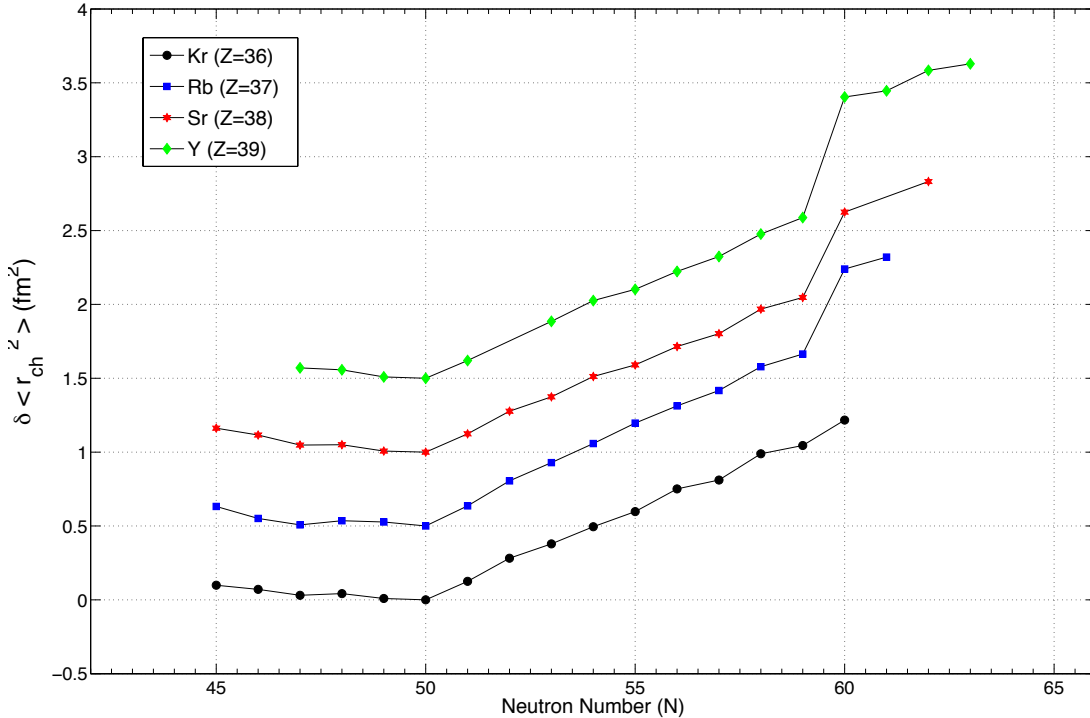


FIGURE 4.1: Changes in Mean Square Charge Radii with respect to the  $N=50$  Shell closure for Kr [44], Rb [41], Sr [45] and Y [46, 47] isotope chains illustrating the deformation occurring around  $N=60$ . The isotope chains have been offset by  $0.5 \text{ fm}^2$  relative to each other for visibility. Errors are smaller than marker size

#### 4.2.2 Recent extensions in measures of MSCR

One of the nuclear properties measured by the Thibault's collaboration was the isotope shift. In order to do so the hyperfine constants and spins were computed from fits to experimental laser spectroscopy data according to the theory described in Chapter 2. The centre of gravity of the  $D_2$  line can then be deduced for an isotope A, which is then compared to a reference spectrum A' which has been previously measured. In the case of Thibault's work  $^{87}\text{Rb}$  was used as a reference isotope due to its stability. The values of the hyperfine coefficients measured by Thibault are presented in Table 4.1 and the isotope shifts in Table 4.2. Equally computed by Thibault are the changes in MSCR

$\delta \langle r^2 \rangle$  whose extraction from isotope shift measurements is described in Chapter 2. Since those results have been published improvements have been made in the calculations of  $F_{el}$  and  $\delta \langle r^2 \rangle^{87,85}$ .

In particular updated  $F_{el}$  was obtained from Dzuba et al. [48] and produce a field shift correction factor of  $-567.45\text{MHz}/\text{fm}^2$  with a 1% uncertainty. The other required parameters to compute Eqn (2.20a) were obtained from Kopferman [49]. In order to extract the  $K_{MS}$  factor it was necessary to use the latest muonic data on stable rubidium isotopes that found the isotope shift between  $^{85}\text{Rb}$  to  $^{87}\text{Rb}$  to be of  $-78.095(12)\text{MHz}$  [50] and  $\delta \langle r^2 \rangle^{87,85} = +0.042(18)\text{fm}^2$  [51]. Substituting these values into Eqn. 2.22 allows us to extract  $K_{MS} = +200.5(37.7)\text{GHz.amu}$ . Using these parameters, updated computations of the change in MSCR can be undertaken as shown in Table 4.2.

As shown in Figure 4.2, the updated computations of the isotope shift using recent atomic factors produce a noticeable shift. In the neutron-deficient region ( $N < 50$ ), previous and updated isotope shifts lie within systematic errors but on the neutron-rich side a significant change is observed. An increasing gradient of change in mean squared charge radii between  $N=50$  to  $N=59$  can be observed along with a more drastic jump at  $N=60$ . This sudden change in trend is identified as the onset of deformation. This sudden onset of deformation at  $N=60$  is also apparent in the yttrium, strontium and krypton isotope chain. Also important to note is that this onset is steeper than that of rubidium's immediate neighbours although direct comparisons between changes in MSCR of elements are difficult as they are highly dependent on systematic errors of the atomic factors used in their determination from isotope shifts.

The change in mean square charge radius  $\delta \langle r^2 \rangle^{87,A}$  and isotope shift  $\delta \nu_{IS}^{87,A}$  with respect to the stable  $^{87}\text{Rb}$  isotope is subject to an increase on either side of the  $N=50$  neutron shell closure. This represents the stability and sphericity of the  $N=50$  shell closure.

From  $^{87}\text{Rb}$  towards the neutron-deficient part of the chain the change in MSCR starts increasing towards a maximum located at  $^{78}\text{Rb}$  which indicates a gradual shape change, a departure from the spherical symmetry of the charge distribution. Magic numbers often indicate regions of stability and sphericity in shape and charge radius. The isotopes  $^{76-79}\text{Rb}$  with  $N=39-42$  are located between the  $N=28$  and  $N=50$  neutron shell closures. This explains the considerable departure from sphericity that their shapes display. This departure from sphericity can equally be seen in the krypton isotope chain for the  $^{72-96}\text{Kr}$  isotopes with  $N=36$  to  $60$  [44].

On the neutron rich side, a rapid, nearly linear growth from  $^{88}\text{Rb}$  to  $^{93}\text{Rb}$  is observed as

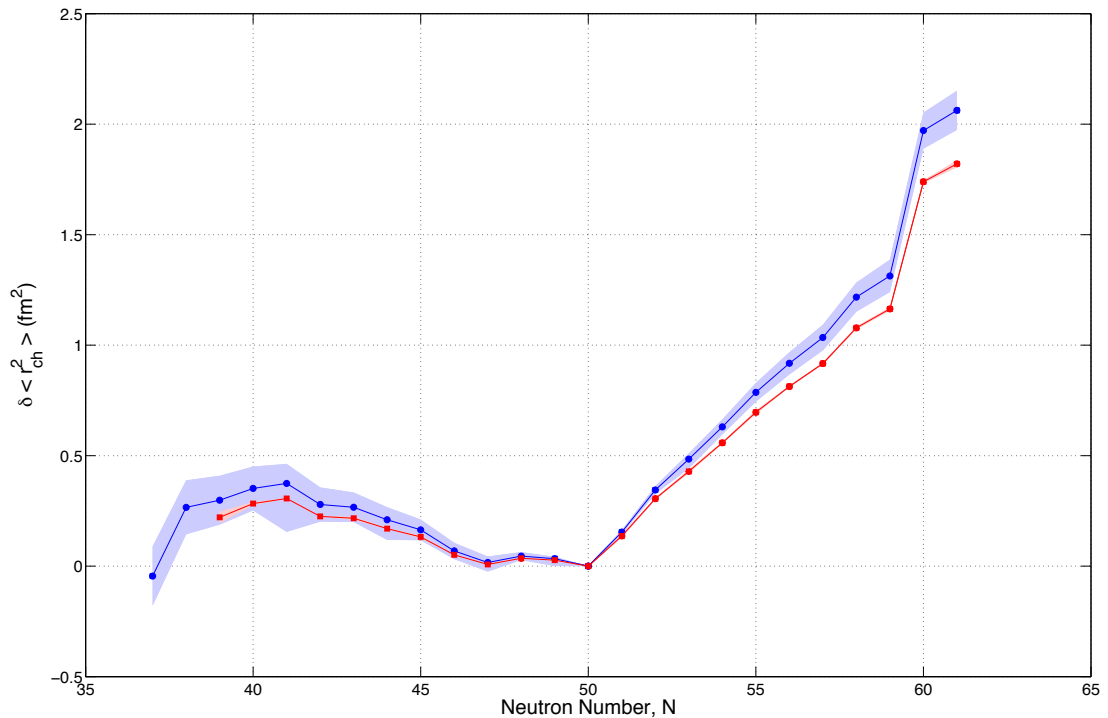


FIGURE 4.2: The change in mean square charge radii of ground state rubidium isotopes from  $^{87}\text{Rb}$  ( $N=50$ ) using Thibault et al [41] (red) and re-evaluated (blue) atomic factors. Systematic error limits that arise from the uncertainties in atomic factors is shown in the shaded blue area.

neutrons fill the sub-shells. Between  $^{96-97}\text{Rb}$  a large increase in the change in MSCR is seen, roughly an order of magnitude bigger than the one observed for the previous eight isotopes in the chain. This sudden and important jump indicates a strong deformation change. This large departure from sphericity can equally be seen in the quadrupole moments  $Q$  which is the largest of the neutron rich side of the Rb chain. Finally Finite Range Drop Model computations by *Möller et al* [54] suggest that several shape isomers coexist in the  $N=60$  region. Both oblate and prolate spherical deformations are predicted with nuclear potentials differing by approximately 1 MeV.

### 4.3 The neutron-rich rubidium program at TRIUMF and its findings

From the analysis of the rotational deformations that arise in the neutron-rich region of the rubidium chain it is clear that beyond  $^{96}\text{Rb}$  the neutron rich isotopes are subject to

A	I	$A(5s^2S_{1/2})$ [MHz]	$A(5p^2P_{3/2})$ [MHz]	$B(5p^2P_{3/2})$ [MHz]	Q [b]
74 <sup>a</sup>	0	-	-	-	-
75 <sup>a</sup>	3/2	719.6(10)	17.8(01)	63(27)	0.669(29)
76 <sup>a</sup>	1	-693(08)	-17.15(02)	32(07)	0.38(0.18)
77	3/2	815.7(5.1)	19.1(1.5)	65.3(3.0)	0.695(32)
78	0	-	-	-	-
78 <sup>m</sup>	4	1185.1(05)	29.3(01)	83.1(22)	0.814(39)
79	5/2	2502.0(0.9)	62.0(0.4)	-9.2(2.1)	-0.098(22)
80	1	-155.2(3.2)	-1.8(2.3)	32.7(1.9)	0.348(20)
81	3/2	2557.6(1.7)	63.8(0.8)	37.4(2.2)	0.398(23)
81 <sup>m</sup>	9/2	2317.3(0.7)	57.9(0.4)	-69.8(5.4)	-0.743(57)
82	1	1031(10)	26.8(3.2)	17.9(6.8)	0.190(72)
82 <sup>m</sup>	5	563.6(0.9)	14.0(0.6)	94.6(11.2)	1.01(0.12)
83	5/2	1061.7(0.6)	26.5(0.4)	18.4(2.1)	0.196(22)
84	2	-1233.7(1.5)	-30.1(0.8)	-1.4(3.3)	-0.015(35)
84 <sup>m</sup>	6	68.2(4.6)	1.2(1.0)	54(26)	0.57(0.27)
85	5/2	1011.0(1.0)	25.3(0.4)	21.4(4.0)	0.228(43)
86	2	-1581.2(1.5)	-39.0(0.8)	18.1(3.0)	0.193(32)
86 <sup>m</sup>	6	563.5(0.3)	14.3(0.4)	34.7(8.9)	0.369(95)
87	3/2	3415.9(2.0)	84.29(0.50)	12.2(2.0)	0.130(21)
88	2	476.2(2.4)	9.4(2.3)	-1.1(9.0)	-0.012(96)
89	3/2	2960.1(0.9)	72.6(1.1)	13.5(2.4)	0.144(26)
90	0	-	-	-	-
90 <sup>m</sup>	3	1003.4(0.4)	25.3(0.4)	19.2(4.2)	0.204(45)
91	3/2	2709.1(1.7)	66.9(1.1)	14.5(2.4)	0.154(26)
92	0	-	-	-	-
93	5/2	1050.2(1.2)	25.8(0.7)	16.6(3.8)	0.177(40)
94	3	930.4(1.1)	23.2(0.6)	15.3(4.7)	0.163(50)
95	5/2	993.7(2.5)	24.0(0.9)	19.8(6.1)	0.211(65)
96	2	1365.2(1.6)	32.9(1.3)	23.1(5.3)	0.246(56)
97	3/2	2286.2(2.6)	55.2(1.8)	54.6(3.1)	0.581(44)
98 <sup>LS</sup>	0	-	-	-	-

TABLE 4.1: A B hyperfine coefficients and quadrupole moments extracted by Thibault et al [41] unless otherwise referenced (a[52]) Statistical uncertainties are placed in parentheses. Empty rows are due to HFS-free I=0 isotopes.

various interesting deformations [55] and so has garnered the interest of the CFBS group for further studies. A survey undertaken at TRIUMF in 2010-2011 has shown that using UCx targets provides sufficient yields for the CFBS experiment to investigate <sup>98</sup>Rb and even heavier isotopes such as <sup>99,100</sup>Rb. This opens the possibility of identifying possible metastable isomers for <sup>98,99,100</sup>Rb, whose existence has been predicted from theoretical computations [40, 42]. Some of the postulated nuclear properties of these ground states and isomers can be found in Table 4.3 [42]. As part of the neutron rich program at TRIUMF <sup>92</sup>Rb was fluoresced and has been subject to calibration runs in December

A	I	$\delta\nu_{IS}^{87,A}$ [MHz]	$\delta\langle r^2 \rangle^{87,A}$ [ $fm^2$ ]	$\langle\beta_2\rangle^2$	$\delta\langle\beta_2^2\rangle$
74 <sup>a</sup>	0	-379(10)	-0.045(18)[134]	-	+0.148
75 <sup>a</sup>	3/2	-519.5(2.3)	+0.266(4)[122]	+0.155	+0.180
76 <sup>a</sup>	1	-502.7(1.9)	+0/298(3)[111]	+0.158	+0.172
77	3/2	-498.6(4.5)	+0.3514(79)[992]	+0.154	+0.167
78	0	-478.4(1.5)	+0.3746(26)[882]	-	+0.159
78 <sup>m</sup>	4	-403.8(1.7)	+0.2431(30)[881]	+0.036	+0.140
79	5/2	-391.6(1.5)	0.2788(26)[774]	+0.001	+0.133
80	1	-352.8(4.4)	+0.2664(77)[669]	+0.150	+0.119
81	3/2	-289.9(1.4)	+0.2099(25)[556]	+0.054	0.099
81 <sup>m</sup>	9/2	-270.4(1.4)	+0.1756(25)[566]	+0.034	+0.094
82	1	-233.7(4.2)	+0.1642(74)[466]	+0.049	+0.081
82 <sup>m</sup>	5	-233.5(3.8)	+0.1638(67)[466]	+0.042	+0.081
83	5/2	-150.1(1.0)	+0.0687(18)[368]	+0.004	+0.056
84	2	-91.6(2.1)	+0.0163(37)[273]	+0.000	+0.037
84 <sup>m</sup>	6	-84(10)	+0.0029(176)[273]	+0.012	+0.035
85	5/2	-78.095(12) <sup>b</sup>	+0.04200(5)[180] <sup>c</sup>	+0.006	0.029
86	2	-45.8(2.0)	+0.0335(35)[89]	+0.007	+0.016
86 <sup>m</sup>	6	-32.1(2.3)	+0.0093(40)[89]	+0.005	+0.013
87	3/2	0	0	+0.006	0
88	2	-61.0(5.1)	+0.1538(90)[88]	+0.000	+0.011
89	3/2	-143.7(2.0)	+0.3448(35)[176]	+0.007	+0.027
90	0	-197.7(5.2)	+0.4843(92)[260]	-	+0.036
90 <sup>m</sup>	3	-188.6(2.0)	+0.4683(35)[260]	+0.003	+0.033
91	3/2	-255.8(2.3)	+0.6300(41)[343]	+0.008	+0.045
92	0	-320.4(5.2)	+0.7862(92)[424]	-	+0.057
93	5/2	-371.5(2.1)	+0.9177(37)[503]	+0.003	+0.065
94	3	-414.7(2.3)	+1.0345(41)[580]	+0.002	0.070
95	5/2	-495.9(3.8)	+1.2174(67)[657]	+0.005	+0.086
96	2	-528.3(4.8)	+1.3134(85) [731]	+0.010	+0.088
97	3/2	-879.7(4.0)	+1.9708(70)[815]	+0.094	+0.172
98 <sup>LS</sup>	0	-910.5(5.3) <sup>d</sup>	+2.0625(93)[885]	-	+0.174
98 <sup>HS</sup>	[3]	-922.5(5.3) <sup>d</sup>	+2.0836(93)[886]	+0.126	+0.177

TABLE 4.2: Isotope shift and change in mean squared charge radius, which were calculated using updated field shift factor and mass shift factors as described previously. Estimated deformation parameters extracted using quadrupole moments and charge radii according to Table 3.1 Extracted from Thibault et al unless otherwise referenced (a[52], b[50], c[51], d[53]). Uncertainties are placed in parentheses. Empty rows are due to HFS-free I=0 isotopes.

2011 by the CFBS experiment in view of using it as a frequency standard for further investigations of the neutron-rich rubidium chain. This particular isotope was chosen as a frequency reference as it possess a known, hyperfine-structure-free  $D_2$  line due to the spin zero of its nucleus and is relatively easily fluoresced.

A	I	$T_{1/2}(ms)$	Decay Mode with Relative Intensity
92	0	$4.492 \times 10^3$	$\beta^- : 100\%, \beta^- n : 0.0107\%$
98	(0,1)	114	$\beta^- : 100\%, \beta^- n : 13.8\%$
$98^m$	(3,4)	96	$\beta^- : 100\%$
99	(5/2)	50.3	$\beta^- : 100\%, \beta^- n : 15.9\%$
100	(3,4)	51	$\beta^- : 100\%, \beta^- n : 5.6\%$
$100^m$	(6)	-	-

TABLE 4.3: Theoretical predictions for neutron rich rubidium chain as evaluated by NuBase-2003 evaluation of nuclear and decay properties [42]. Parentheses indicate tentative assignments. The only property listed for  $^{100m}\text{Rb}$  is the spin according to [40]

In order to assist experimental runs, where time is limited, predictions of both the hyperfine peak energies and isotope shift predictions were undertaken prior to the run. Isotope shifts were performed using cubic spline interpolations using values from Thibault. The interpolated function is then extrapolated using a monotonically decreasing second degree polynomial for values of hyperfine coefficients A below 105. Using this extrapolation, isotope shifts for  $^{98-100}\text{Rb}$  are predicted as -932.3, -1036 and -1111 MHz respectively. These predictions and how they were obtained are discussed in detail in [56]. Centroid energies for the hyperfine peaks are computed using equation 2.28 using predicted spin assignments along with a beam energy value of 20keV. Predictions of A coefficients for  $^{99,100}\text{Rb}$  are linearly extrapolated from  $^{97,98}\text{Rb}$ . B coefficients were set to zero for these predictions as they have quite a small contribution. Even if this method is far from precise, these predictions are still useful, especially for rubidium as in the relatively small scale of the hyperfine splittings, which are of the order of 1 GHz, a change of an order of magnitude in A coefficients only corresponds to an energy shift of the order of 10 V applied to the Doppler tuning electrodes. Typical voltage sweeps are of the order of a couple of hundred volts which easily encompasses the uncertainty on the predictions. In order to make best use of the experimental time, the voltage scans were devised taking into account the beam energies, the hyperfine splitting energies as previously predicted and laser wavenumber in order to set the optimal Harrison bias voltage ( $V_0$  in Eqn 3.11). Using the optimal set voltage allows for the whole predicted hyperfine peak spectra to be covered within a single scan sequence. If the isotope of interest has low yield (less

than  $10^5$  ions per s) as was the case for  $^{98}\text{Rb}$  then two separate scans can be undertaken to investigate the low and high frequency triplets separately. This allows for greater statistics and resolution on the region of interest without having to scan the empty frequency space between the structures.

Two long lived nuclear states for  $^{98}\text{Rb}$  have been postulated [40]. One has a low spin and had been tentatively assigned to  $I=0$  by the Thibault et al rubidium laser spectroscopy survey [41]. The other is a previously unobserved high spin (HS) state. The HS state had tentatively been determined to be the ground state with  $I = 3^+$  from gamma decay experiments [57]. During experimental runs in November 2012 and July 2013 the CFBS experiment at TRIUMF successfully and unambiguously observed two distinguishable nuclear states for which the optical spectrum is shown in Figure 4.3. Unfortunately due to the nature of the optical measurements it is impossible to determine the excitation energies of these two states and assign them as the ground or isomeric state. In order to describe them, as their spin have equally not been formally assigned by other experiments sensitive to excitation energies, they will be referred to as high spin HS and low spin LS states.

The two  $^{98}\text{Rb}$  states have comparable spectral intensities which points to similar yields, leaving open the possibility of mass measurements on these two states. The lifetimes of these two states were measured in the experiment using variable trapping times of the RFQ. The lifetimes of the two states were found to be similar and around 100 ms. The central frequency structure is assigned as the LS state as it possesses only one transition, characteristic of  $I=0$  states. The structure is fitted with a single Voigt peak as described in section 3.3.1 with FWHM of approximately 35 MHz. This FWHM and the properties of the Voigt profile for the LS state were similar to other  $I=0$  states such as  $^{92}\text{Rb}$  and the single transitions present in the stable  $^{85,87}\text{Rb}$ . This helps rule out  $I > 0$  state, which can take the form of a collapsed structure with tight energy spread. The isotope shift was computed with respect to the  $^{92}\text{Rb}$  frequency standard isotope from the fitting routine by computing the centroid positions of the structures. These shifts were then used to obtain the isotope shift with respect to  $^{87}\text{Rb}$  presented in table 4.2. Therefore the CFBS group has unambiguously confirmed that  $^{98}\text{Rb}$  possess a  $I=0$  LS state.

The HS state, the outer structure on the spectrum in Figure 4.3, was fitted using a  $\chi^2$  minimization routine using a multiple peak Voigt profile along with different assumed nuclear spin values.  $I=0$  was excluded due to the split nature of the spectrum and

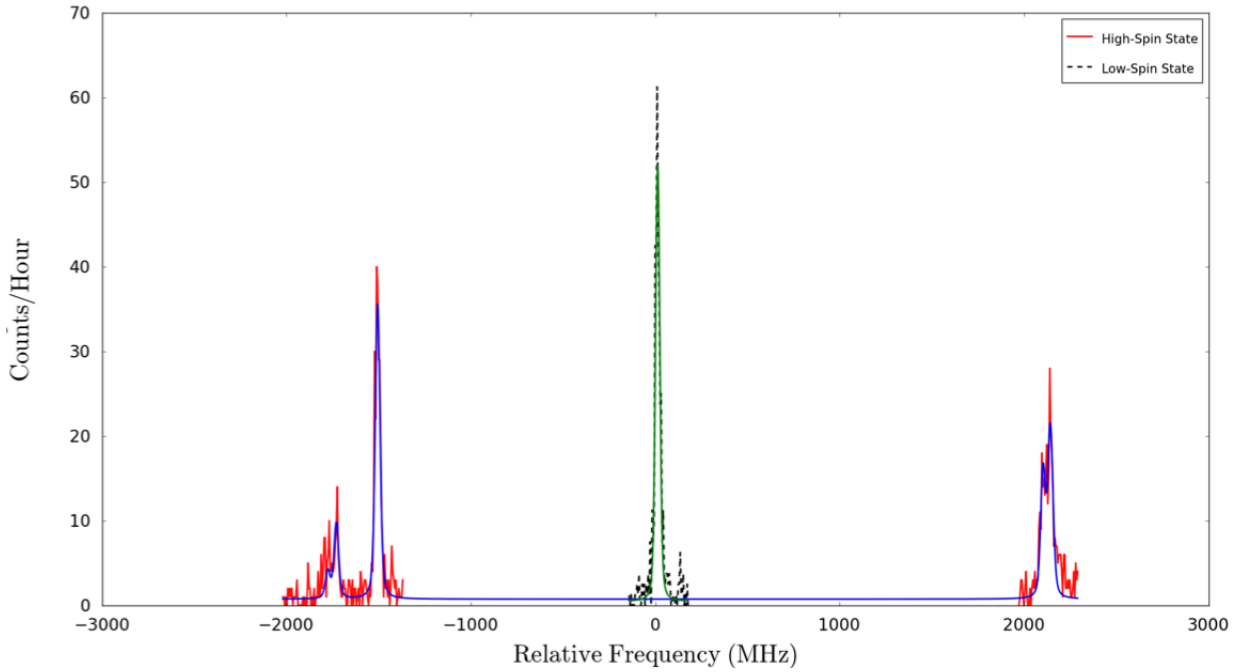


FIGURE 4.3: Optical spectrum for  $^{98}\text{Rb}$ , measured on the D2 transition, showing the two observed nuclear states. The low-spin state and each side of the high-spin state were individually scanned; the normalized count rate is given to represent their relative intensities. Fits of the low- and high- spin states with  $I = 0$  and  $I = 3$  respectively are included (solid lines).

the visible multiplicity of the peaks.  $I=1$  and  $2$  were excluded as their ratios of fitted A hyperfine coefficients ( $\frac{A(5s^2S_{1/2})}{A(5p^2P_{3/2})}$ ) are inconsistent with expected values from other rubidium isotopes [41]. The predicted ratio obtained from other accepted values for isotopes in the rubidium chain is of  $+40.3(1)$  as opposed to the ones for  $I=1$  or  $2$  which give  $35.0(3)$  and  $38.0(3)$  respectively. The fitting routine was then undertaken for the other spin assignments using background, hyperfine coefficients and peak intensity as free parameters. Constraints added to this fitting routines are relative peak intensities calculated by angular momentum couplings obtained from [58] and FWHM of individual hyperfine peaks from the experimental values of the  $^{92}\text{Rb}$  experimental scans. Superior reduced chi squared,  $\chi_r^2$  values for  $I=5$  and above along with inconsistent values for the ratios of fitted A hyperfine coefficients ruled these possibilities out. Nonetheless similar values for both  $I=3$  and  $4$  as seen in Table 4.4 made it difficult to firmly assign a spin to the HS state. Equally helping us discount the  $I > 4$  spin assignments are the gamma decay spectroscopy measurements of  $^{98}\text{Rb}$  into  $^{98}\text{Sr}$ [57] due to strong beta feeding into the  $K=3$  level in Sr. The reason the fitting routine was unable to predict a better spin assignment is the overlapping peaks in the spectrum, which make individual hyperfine

A	I	$\chi_r^2$	$A(5s^2S_{1/2})$	$A(5p^2P_{3/2})$	$B(5p^2P_{3/2})$	$\delta\nu_{IS}^{92,A}$
			[MHz]	[MHz]	[MHz]	[MHz]
$98^{LS}$	0	0.86				-590.1(0.9)
$98^{HS}$	[3]	1.02	+1108.5(0.6)	+27.51(0.07)	+134.5(2.7)	-602.1(1.2)
$98^{HS}$	[4]	1.04	+864.3(0.5)	+21.45(0.06)	+157.5(3.0)	-546.8(1.2)

TABLE 4.4:  $^{98}\text{Rb}$  experimental measured hyperfine A and B coefficients, isotope shifts and associated  $\chi_r^2$ .

transitions difficult to discern. Once the hyperfine spectrum is fitted the hyperfine coefficients can be extracted [19] and are presented along with the associated fit  $\chi_r^2$  in table 4.4.

Having identified  $I=3$  and 4 as possible spin assignments based on fit  $\chi_r^2$  values, we have tentatively assigned the HS state as  $I=3$  as it possesses favourable positive parity although  $I=4$  spin assignment cannot be discounted as the  $2^+$  level in Sr could be fed by low spin states of  $I=1$  and the difference in associated  $\chi_r^2$  are inconclusive.

# Chapter 5

## Laser Locking Program

### 5.1 Motivation and Overview

The CFBS group at TRIUMF relies on the short term (seconds and less) and long term (hours to days) stabilization of its excitation laser frequency in order to produce a precise measurement of the hyperfine energies of the nuclides it studies. Short term stability and line-width controls require large feedback bandwidths whilst long term stability needs gain at very low frequency extending to DC. Often short term stabilization is undertaken by the manufacturers of the frequency stabilized lasers used in these experiments using optical and electronic methods but the long term stability is generally left to the user. The reason laser frequencies tend to drift over longer periods of time is related to environmental effects on the laser's optical resonator. When the temperature, air pressure or humidity changes it affects the size and properties of the resonator which in turns leads to drifts in the lasers wavelength. The MBR laser employed by the CFBS group as an excitation laser has been found to exhibits drifts of the order of the 100MHz over one hour [59]. The line-widths of the hyperfine structures investigated by the CFBS group are of the order of 35MHz. Due to the low production rates of the rare isotopes investigated and the need for significant statistics for peak fitting, the duration of scans of hyperfine structures are of the order of days. Given the duration of these scans, the frequency drifts of the MBR and the small line-widths of the investigated hyperfine structure it is necessary to implement a long term laser frequency stabilization protocol.

A common solution for the implementation of long term frequency stabilization involves

sending a feedback signal to the frequency control of commercial lasers to lock the laser to either a sharp atomic transitions [60] or a cavity fringe of a stabilized Fabry-Perot interferometer [61]. The latter of these techniques is employed by the CFBS group as it affords more versatility to the laser system which allows for easier investigation of a wider array of elements. The long term stability of a reference laser is effectively transferred to the MBR using a Fabry Perot resonator. The reference laser employed by the CFBS group is a helium-neon (HeNe) laser whose frequency has been stabilized by matching the intensities of two orthogonal polarization modes [62]. The HeNe has typical frequency drift of  $\pm 0.8$  MHz in one hour and  $\pm 1.2$  MHz in eight hours [63].

## 5.2 Frequency stabilization apparatus

Figure 5.1 shows the schematic diagram of the laser frequency control system. It possess three components: a scanning CFP cavity, the stabilized laser system and a data acquisition/digital feedback control module. The CFBS group employs a CFP interferometer as it presents many advantages in the context of laser spectroscopy [64].

The principal difference between the CFP and the flat plate Fabry-Perot is that instead of using two parallel partially transmitting mirrors to create its resonant cavity, the CFP uses two partially transmitting spherical mirrors that have equal radii of curvature. The mirrors are separated a distance equal to that radius. The optical axis runs through the centre of the mirrors and the foci of the mirrors are at the centre of the Fabry Perot. After four reflections in the CFP the light starts to interfere with itself with each successive roundtrip and the resonant light is emitted at the second mirror. The path an optical ray follows in a CFP is shown in Figure 5.2. The incident light is transmitted through the first mirror and travels inside the cavity to the second mirror where it is reflected and passes through its focal point back to the first mirror. The light is then reflected off the first mirror via its focal point to the second mirror and then back against the first mirror completing its four reflections in the cavity. These four reflections in the cavity constitute one iteration. The resonance condition occurs when the total internal CFP cavity path length is equal to an integral number of wavelengths of the light travelling through the cavity which results in constructive interference. When this constructive interference occurs, the length of the cavity  $L$  will be an integer number of

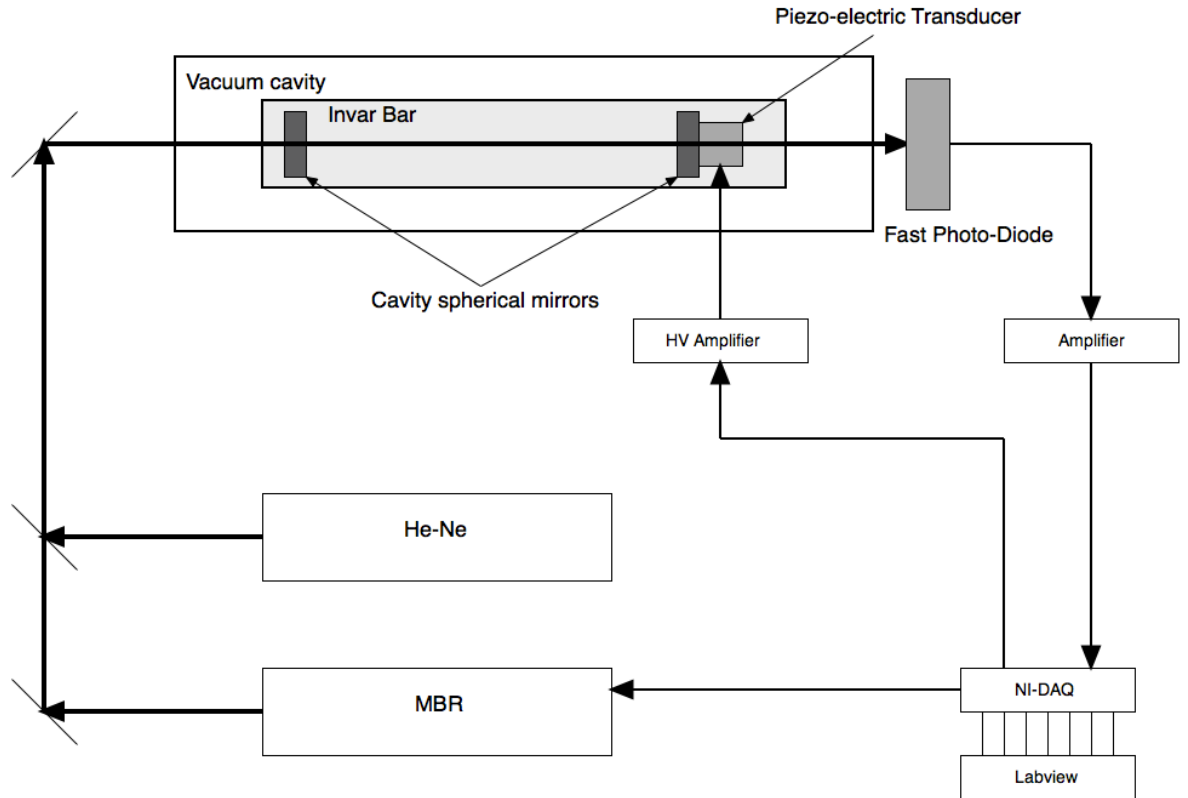


FIGURE 5.1: The schematic diagram of the locking apparatus

quarter wavelengths of the resonating frequency [65]:

$$L = \frac{m\lambda}{4} \quad (5.1)$$

where  $m$  is the index of cavity mode an integer greater than 0 and  $\lambda$  the wavelength of the light. This expression can be solved for the permitted frequencies  $\nu$ :

$$\nu_m = \frac{mc}{4nL} \quad (5.2)$$

with  $c$  the speed of light and  $n$  the index of refraction inside the CFP. Therefore the difference between adjacent permitted frequencies or Free Spectral Range (FSR) is:

$$\Delta\nu_{cfp} = \nu_{m+1} - \nu_m \quad (5.3a)$$

$$\Delta\nu_{cfp} = \frac{c}{4nL} (\text{Hz}) \quad (5.3b)$$

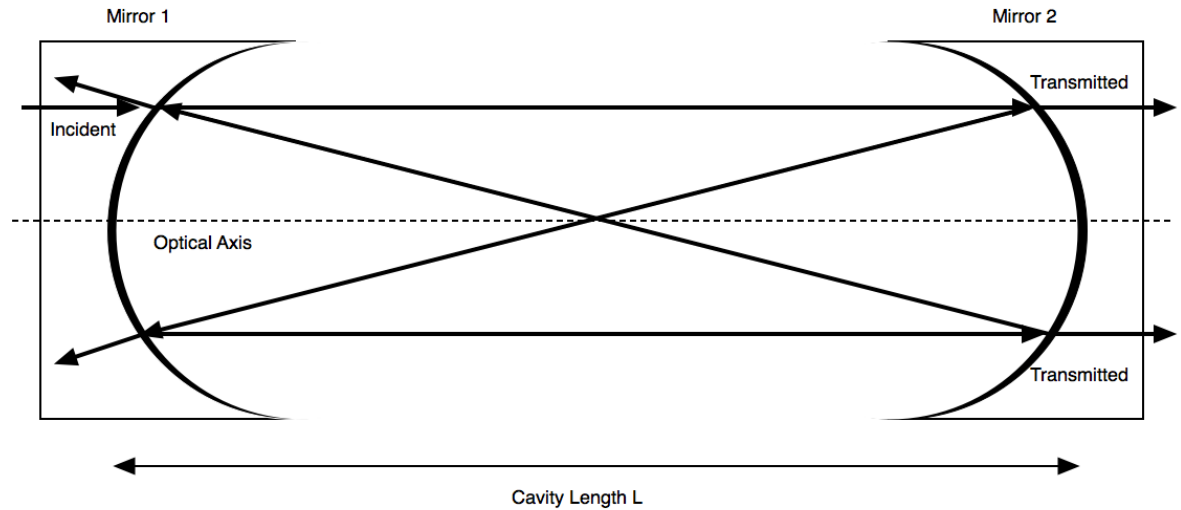


FIGURE 5.2: Diagram of the Confocal Fabry Perot and the path taken by the Light in its Cavity

The incident light enters the CFP cavity and undergoes multiple reflections between mirrors and interferes with itself over many iterations. If the frequency of the incident light is such that constructive interference occurs within the CFP cavity then the light will be transmitted out of the cavity via the second mirror in the form of resonant peaks that can be read on a fast photodiode. Destructive interference will not allow any light out of the CFP cavity which in practice gives us a very precise frequency filter.

If the cavity had a fixed, un-variable size it would only transmit at multiples of a fixed frequency. So the CFP in a scanning configuration possess a mirror mounted on a piezo electric transducer (PZT), which by applying a variable generated voltage allows the controllable and incremental change in the cavity length  $L$ . Typical voltages used to scan the PZT are of 0 to 800V. Whilst scanning the cavity length, the transmission peaks can be visualized on a detecting photodiode. This cavity length scanning allows it to act as a narrow tuneable band pass filter for our laser light. The filter is precise up to the finess of the etalon as it is necessary to resolve the transmission peaks. The

PZT mounted mirror is scanned over a certain length  $L$  by voltage ramp, corresponding to a FSR for the  $\lambda = 633$  nm HeNe laser. Both laser beams, the HeNe and the MBR are directed and mode matched into the CFP etalon in order to obtain a transmission spectrum as the one shown in Figure 5.3 which displays one HeNe FSR along with one MBR transmission peak.

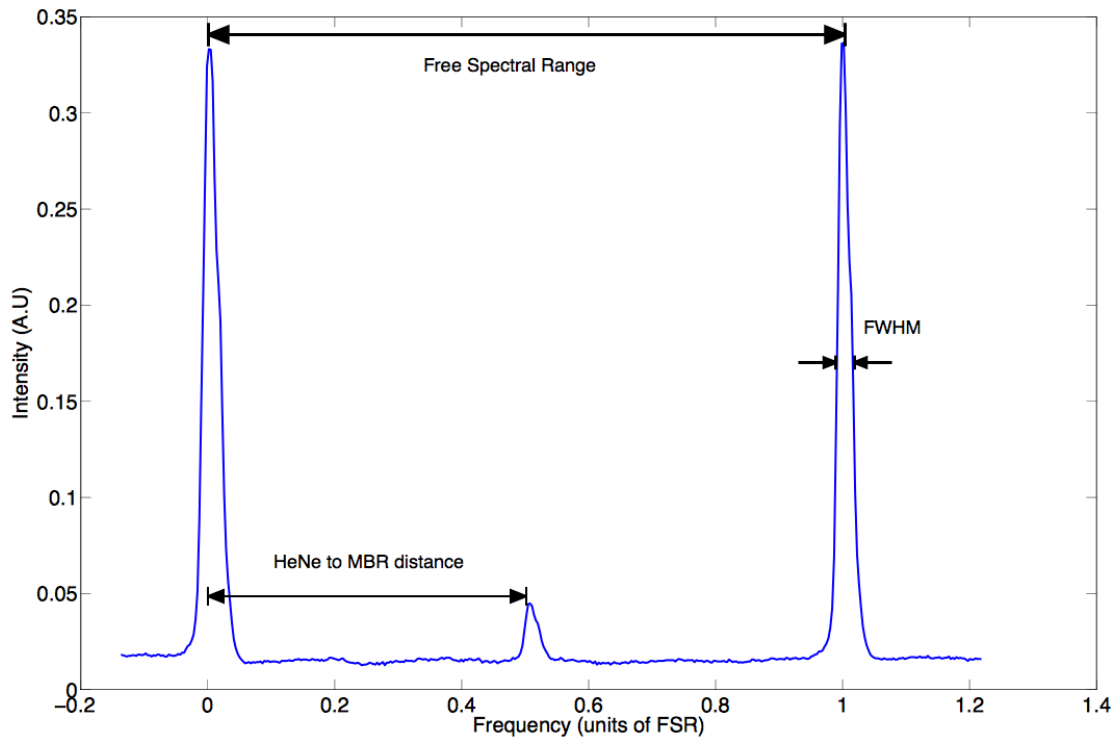


FIGURE 5.3: Typical spectrum from the diode showing transmission peaks for the reference HeNe and the MBR. The frequency axis is normalized in such as way that the consecutive HeNe peaks that constitute a FSR are assigned 0 and 1 respectively. The FSR, FWHM and distance between the HeNe and MBR peak are indicated on the plot.

Whilst this controllable variation in the length of the cavity is essential for the use of the CFP, unwanted and uncontrollable variations lead to errors in frequency readings that jeopardize the locking mechanism. One such important source for cavity length variations is the thermal expansion of the CFP material. Care must be taken whilst selecting this material to ensure a low expansion coefficient. Even so, metals still have a non zero coefficient of expansion so the length of the cavity will slowly lengthen with temperature and cause uni-directional drift of the the resonant frequency that may lead to the mode jump of lasers that can cause havoc in laser locking protocols. The CFP employed by the CFBS experiment is based on a cavity bored into an Invar bar which has

a low coefficient of expansion ( $1.2 \times 10^{-6} \text{K}^{-1}$ ) [66]. The temperature instability change in the length of the cavity is given by [67]:

$$\Delta L = \Delta T \alpha L \quad (5.4)$$

with  $\Delta L$  the variation in cavity length,  $\Delta T$  the temperature change and  $\alpha$  the coefficient of expansion of the cavity material. Due to these shifts the resonant frequency shift of the interferometer  $\Delta\nu$  can be expressed as:

$$\Delta\nu = \frac{c}{4L} \times \frac{L\Delta T\alpha}{\lambda/4} \quad (5.5)$$

with  $\lambda$  the laser wavelength. It is clear from Eqn 5.5 that if the accuracy of the frequency stabilization is required in a range of a few MHz then much care must be taken whilst selecting the material for the cavity. Also efforts must be undertaken to isolate the CFP from thermal fluctuations either passively with temperature controlled rooms and insulation or actively using temperature controls. The CFBS's CFP is sealed and pumped to vacuum to insure uniform index of refraction in the cavity but also to limit thermal fluctuations. A second important parameter describing the performance of the CFP is the finesse. The finesse relates to the frequency resolution of the CFP and can be written as [68]:

$$F = \frac{FSR}{FWHM} \quad (5.6)$$

where FSR is the Free Spectral Range and FWHM is the Full Width Half Maximum of the transmission peak of the CFP. The finesse is a dimensionless quantity and so the FSR and FWHM used to compute it must possess the same units. Etalons with high finesse show sharper transmission peaks. The finesse of the the CFP etalon for the HeNe frequency is of  $F=31$ . The transmission peak from an etalon dependant on the mirror reflectance  $R$  such that [69]:

$$T = \frac{(1 - R)^2}{1 + R^2 - 2R\cos\delta} \quad (5.7)$$

with  $\delta$  the phase difference between successive transmitted pairs of iterations in the CFP.

### 5.3 Laser Locking with LabView: Data acquisition and feedback control

Having discussed the critical importance of the laser frequency lock and the hardware employed to ensure the most reliable lock, the program developed to lock the laser is introduced. The CFBS group has chosen to develop its new laser locking program in National Instruments LabView for a variety of reasons. The integrated input/output capabilities that National Instruments provide, along with the fast Data Acquisition boards (DAQ) that allow control over all the parameters of the laser locking without the limitations of slow USB connections. It allows simultaneous and synchronous voltage ramp generation to scan the CFP, acquisition of laser peak positions and feedback. In order to improve the laser locking precision the previous USB NI-DAQ unit has been replaced by a DAQ board, the NI PCI-6221 16-bit (37 Pin) [70] which not only improves data transfer from locking software to hardware but also provides more inputs ports. These allow for more complimentary diagnostics for the laser locking system along with the possibility to expand the set-up in the future by simultaneously visualizing multiple lasers independently on different photodiodes.

Another important reason LabView was chosen as environment to develop the laser locking program was the intuitive graphical interface of it's front panel. Data can be visualized in real time, whilst being logged. The easy-to-use front interface allows many users to manipulate the program for the purpose of laser locking during experimental runs without extensive training or understanding of the inner workings of the program. This is of particular interest to the CFBS group which is a collaboration with members from different institutions. The various members can come in during experimental runs and very quickly manipulate the program and acquire data without the need to be present at TRIUMF for long periods prior experimental runs to familiarize themselves with the ever-evolving experimental set-up.

If the laser lock is lost during the run the ensuing hyperfine spectra data is unusable. Real time visualization is used to track and characterize the lock and re-lock the laser as soon as its frequency drifts or its mode hops. The measurement of excitation frequency used in the analysis of hyperfine structure is assured by an independent high precision Bristol Instruments 621 series wave-meter which is accurate to  $\pm 0.0002$  nm at 1000 nm. The laser locking program is mainly implemented to stabilize the frequency and counter

MBR drift as opposed to measure the absolute frequency value.

The program generates the voltage ramp to drive the PZT over a distance  $L$  in order to obtain the spectra of cavity fringes. The data acquisition continuously reads the analog-to-digital converter (ADC) associated with the photodiode signal synchronized with the cavity scan. Each ramp cycle consists of 1000 equally distributed data points corresponding to a ramping rate of a 100Hz. During each cycle the program acquires spectra associated with the increasing voltage scan, therefore our spectra represent photodiode output in function of voltage scan number. The program then proceeds with obtaining the position of each spectral peak. The two HeNe transmission peaks that define a FSR are initially coarsely fitted. For the first HeNe peak, a decreasing linear function is added to the spectrum. The two HeNe peaks being of similar intensity and the MBR peak's intensity being relatively small, the addition of this linear function makes sure the first HeNe peak is clearly the maximum of the spectrum. The slope of the linear function must be calibrated in order to assure the reliable identification of laser peaks. Once the calibrated slope has been determined for which the maximum of the spectrum is always located at the first of the HeNe peaks, the position of the spectrum maximum is then extracted. Similarly for the second HeNe peak, an increasing linear function is added to the spectrum which makes of the second HeNe peak the maximum of the spectrum. Again the position of this maximum is extracted. A finer fit of the HeNe peaks' positions are then undertaken using a centre of gravity calculation on a restricted region around the previously determined coarse HeNe peak positions.

Once the peak positions have been determined, the FSR is computed by taking the difference between consecutive He-Ne peak positions. The MBR peak position is then computed similarly by finding the spectrum maximum in the region between the two HeNe peaks that constitute the FSR. Then employing a centre of gravity calculation on a restricted region around that maximum to obtain a precise value of the MBR peak position. Using a centre of gravity computation to obtain spectra peak positions was a choice made during the development of the program as it was found that trying to fit the etalon transmission line-shape (Eqn. 5.7) to the spectra peaks considerably increased the delay of data analysis time. The program was significantly slower, which increased our frequency drifts for marginal improvements on peak position.

The sequence that the laser locking program undertakes is schematically illustrated in

the block diagram shown in Figure 5.4. First the Laser Locking Program generates and sends a voltage ramp to the PZT in the CFP which scans the cavity length  $L$  to obtain the spectra of cavity fringes from the fast photodiode. The NI DAQ board and LabView are used to synchronize etalon cavity voltage ramp generation and data acquisition at a ramping rate of 100 Hz. The computer monitor continuously displays the spectra for the user to see. After each scan the program calculates the laser peak positions as previously described. The user can then use a set manual steps of variable magnitude to alter the cavity FSR by changing the magnitude and offset of the generated voltage ramp from the NI-DAQ board. The MBR laser frequency can equally be manually shifted by changing the voltage bias sent to the MBR controller. In this fashion the user can simply, intuitively and in real time set the initial parameters for the experimental run prior to locking the laser frequency.

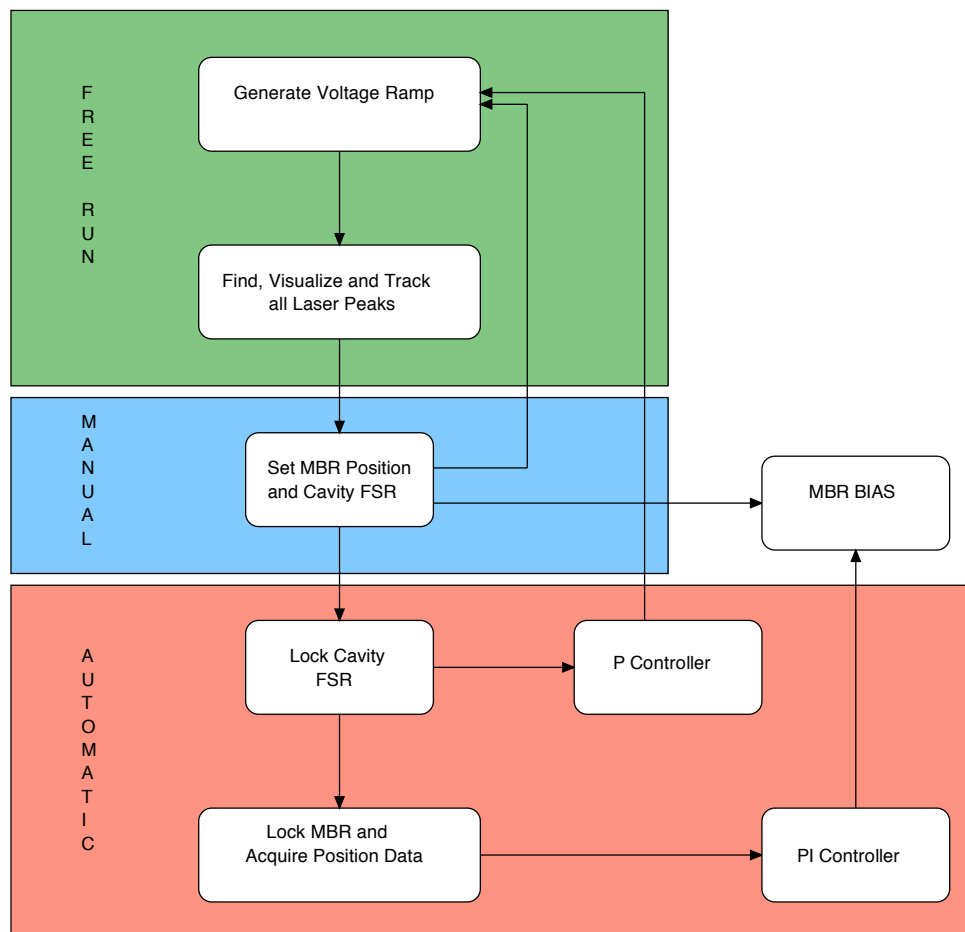


FIGURE 5.4: Block Diagram of the LabView Laser Locking Program which controls cavity scans, data acquisition and laser frequency

The difference between the MBR peak and the first HeNe peak is then computed to obtain our set-point (SP) for laser locking. Peak separation is then maintained at a desired fixed SP value using a feedback loop to the MBR's frequency controller. Drifts from the set-point contribute to the error signal  $e(t)$  used for the digital feedback loops:

$$e(t) = SP - CV \quad (5.8)$$

with  $CV$  the current value of the MBR to HeNe peak separation. The NI DAQ board can send voltages ranging from  $\pm 10V$  via a digital to analog converters (DAC) which controls the variable frequency range of the MBR controller. This frequency range is optimized by the user in order to obtain a DAC step best suited for the laser stabilization feedback loops. For the measurements undertaken and presented in this thesis the scanning range of the MBR controller was set to 4 GHz. Once the experimenters are satisfied with the cavity FSR span they can engage the variable feedback loop to lock the FSR. Locking the FSR keeps the distance between the two HeNe peaks constant in order to have the system referenced to the same successive HeNe modes. This is achieved by varying the generated voltage ramp used to drive the PZT. The feedback loop consists of a proportional controller (P). The error signal used for the proportional controller is the difference between the FSR at the last iteration and the current one. The proportional controller outputs a feedback value proportional to the current error signal. The magnitude of the response can be adjusted by multiplying the error by a constant  $C_p$  called the proportional gain constant. The proportional feedback  $F_P$  is given by [71]:

$$F_P = C_p \times e(t) \quad (5.9)$$

where  $e(t)$  is the error signal for this iteration. The  $C_p$  term is tuned in order to output the optimal feedback for our system. Manual tuning was undertaken for the P controller, if the FSR is seen to oscillate around the SP, the  $C_p$  term was decreased. If the FSR was seen to drift away from the SP, the  $C_P$  term was increased. In this way an optimal  $C_p$  term for this feedback loop was obtained. Once the FSR has been locked using the proportional controller the MBR frequency can be locked. In order to do so a proportional-integral controller is employed to afford greater stability. Proportional controllers requires a non zero error to drive it and so it has a tendency to operate with a steady state error. In order to counter this an integral term  $F_i$  can be added to the P

controller to form a proportional-integral (PI) controller. Integral controllers introduces "memory" to the feedback loop. The integral term is the sum of the instantaneous error of each iteration over a user defined time  $t$  in order to account for accumulated offset that should have been corrected previously. This accumulated error is then multiplied by an integral gain constant  $C_i$ .  $F_I$  has the form [71]:

$$F_I = C_i \int_0^t e(t) dt \quad (5.10)$$

The integral term accelerates the feedback towards the desired set-point and eliminates the unwanted residual steady state error from the proportional controller. Care must be taken to tune the integral gain constant  $C_i$  and the integration time as the integral controller can overcompensate for previous error and overshoot the set-point. In such a way that the long term stability of the excitation laser frequency can be achieved.

## 5.4 Performance of the laser stabilization system

### 5.4.1 The free spectral range of the confocal Fabry-Perot

In order to quantify the stability of the developed system it is necessary to convert the transmission peak positions of the CFP etalon obtained via the stabilization program into a MHz. In order to do this a precise measure of the HeNe FSR was employed. The distance between successive HeNe peaks defines the FSR and is kept constant by the laser locking program (LLP) feedback loop. The x-axis of the transmission spectra seen on the photodiode are in units of voltage ramp step. Assigning values of 0 and 1 to the first and second HeNe peak positions that define the FSR as seen in Figure 5.3 converts the x-axis into units of HeNe FSR. In order to obtain the frequency drifts of the MBR in MHz, the FSR must then be calibrated and converted to MHz. To achieve this, an Electro-Optic Modulator or (EOM) was used to create sidebands in the monochromatic reference HeNe laser beam [72]. The EOM relies on the electro optic effect. This effect changes the refractive index of a crystal when subjected to a DC or time varying radio frequency (RF) signal thereby causing a phase shift in the optical signal. When the control voltage is a time varying signal, the optical beam undergoes frequency modulation, some of the energy of the fundamental frequency  $f_0$  is converted into sidebands separated from the fundamental frequency by integer multiples of the modulating frequency  $f_m$ . So these

sidebands have frequency  $f$ :

$$f = f_0 \pm n f_m \quad (5.11)$$

The amplitude of the sidebands with respects to the fundamental frequency can be influenced by the amplitude of the applied voltage and are given by the Bessel functions. In this way it is possible to add a single pair of symmetric sidebands about the reference HeNe laser by calibrating our RF voltage generation in such as way that only the first order sidebands and fundamental peaks are visible. As these are first order sidebands they are located exactly  $f_m$  away from the fundamental frequency. These sidebands are present on either side of both the HeNe peaks visible in the FSR. The radio frequency driver used for this is programable to output user defined frequencies in MHz which allows us to convert FSR units into MHz. The two HeNe peaks that constitute a FSR and their associated sidebands are shown in Figure 5.5.

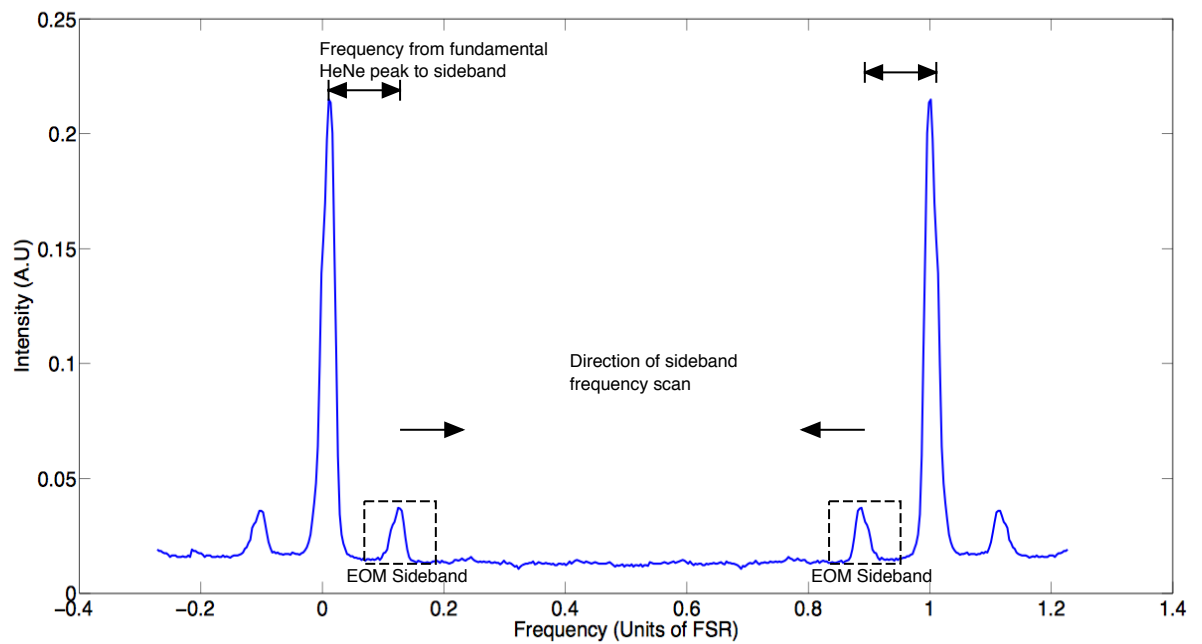


FIGURE 5.5: Illustration of EOM generated sidebands on the HeNe laser spectrum. The sidebands are an equal distance in absolute frequency to their central HeNe peak. By discretely scanning the RF frequency we can step the sidebands until they overlap and determine the CFP etalon FSR.

The intensity of the sidebands depends on the intensity and the frequency of the applied RF. For these frequency calibrations the intensity of the RF was kept constant in order

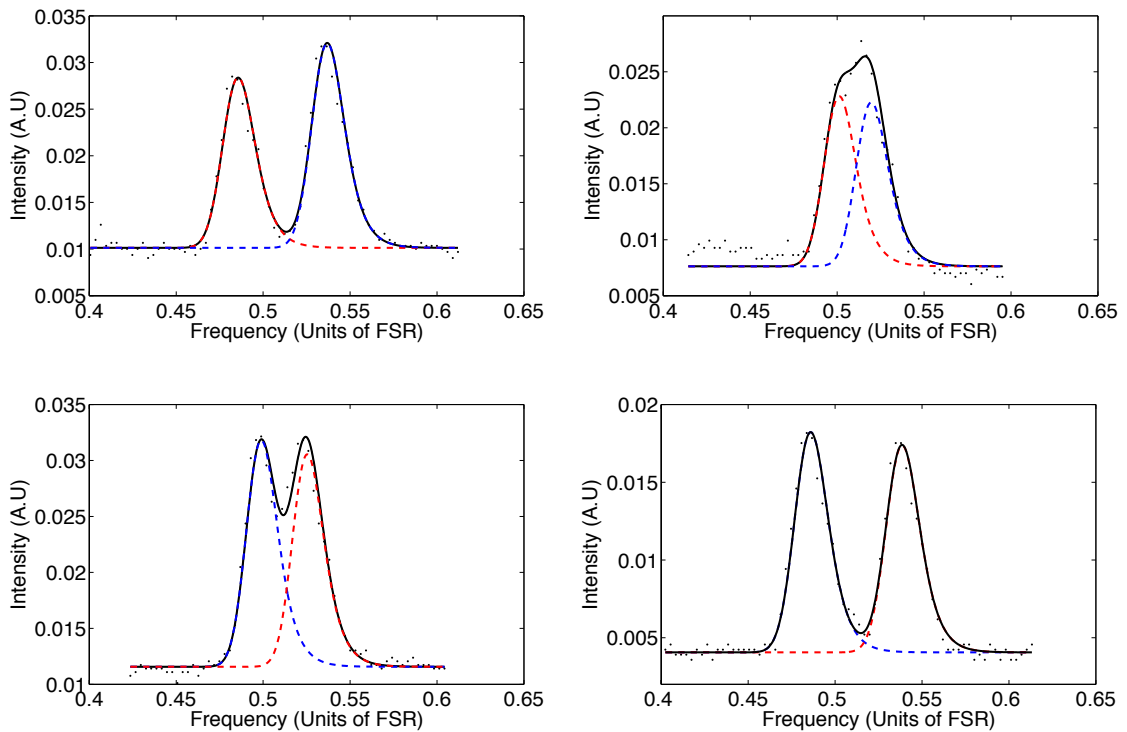


FIGURE 5.6: Fitting the overlapping HeNe sidebands. The red and blue fits are associated to the sidebands from either side of the FSR. The black fit is the overall fit. These data sets go clockwise in increasing sideband frequency

for the EOM amplitude modulation to remain constant and only the first order sidebands remain visible. By stepping the RF frequency and fitting the sideband position it is possible to obtain the sidebands position in units of FSR. As the EOM parameters were kept constant, the function used to fit the sidebands has the same width and line-shape. The line-shape was obtained from a sideband at a frequency unperturbed by the neighbouring peaks. The optimal function that best describes the line-shape for fitting purposes was determined to be an exponentially broadened gaussian even if it theoretically is a weighted sum of Lorentzians. The exponential broadening was needed to account for the slight asymmetry visible in all the CFP transmission line-shapes due to the way the light was aligned into the cavity and nearly degenerate TEM modes. As the RF frequency increases and approaches half the FSR of the CFP, the sidebands overlap in the middle of the spectrum as shown in Figure 5.6. This overlap coincides exactly with half the FSR. In order to determine the FSR of the CFP in MHz the sideband frequencies were scanned, in 1 MHz steps from 140 MHz to 160 MHz about the expected FSR/2 value of 150 MHz. A 20 MHz range about the overlap was taken and the two

sidebands fitted simultaneously using a double exponentially broadened gaussian line-shape with the parameters extracted from the initial single sideband. In this way only the peak position and height were left as free parameters. The centroid position of the sidebands are then extracted from the fits along with the associated fit error. A illustrative selection of fits in Figure 5.6 show the two sidebands overlapping when scanned across RF frequencies spanning the centre of the CFP FSR. Once centroid positions and associated errors for the two sidebands were obtained they are fitted using linear regression. The centroid positions and their error in units of FSR are plotted against the RF frequency along with the associated linear fits as shown in Figure 5.7. Using the linear fits we determine the frequency at which the sidebands cross and that will give us a measurement the distance between the HeNe peak and the middle of the FSR or half the FSR with an associated propagated error. Using this method the FSR of the CFP was found to be of 300.2(8) MHz.

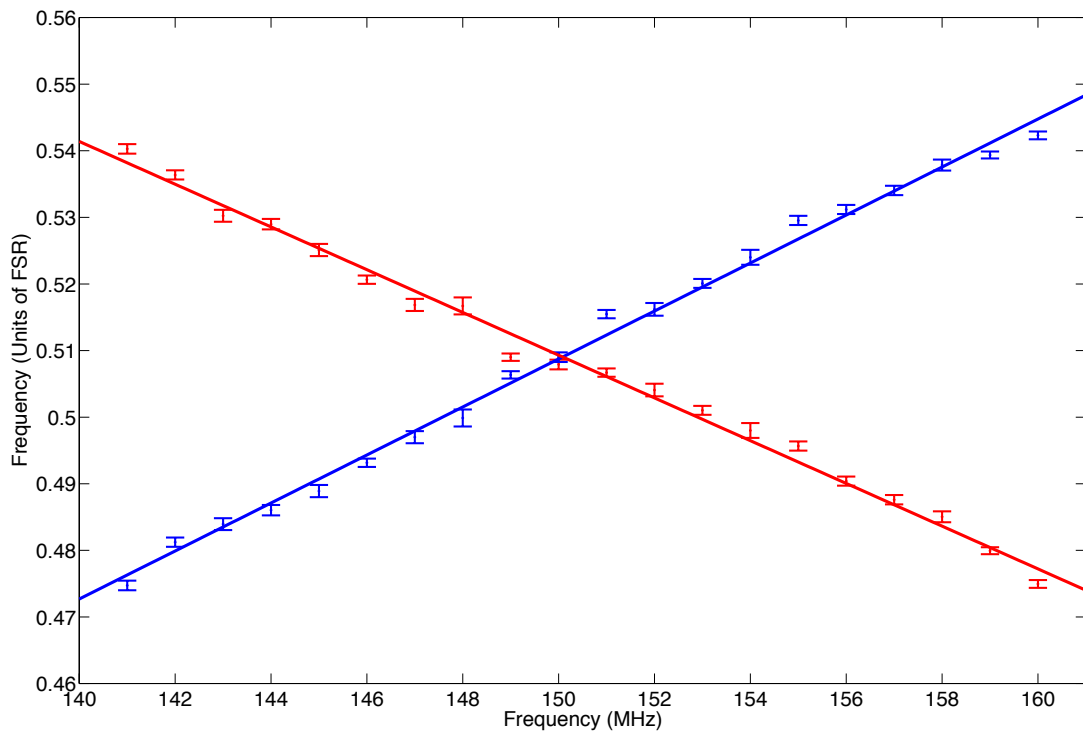


FIGURE 5.7: FSR units in function of HeNe sideband centroid frequency used to determine the FSR of the CFP etalon in MHz. The error-bars are obtained from the centroid peak fitting but could also be a result of PZT hysteresis. Equally plotted are the associated linear fits of the sideband centroid frequencies.

With the FSR of the CFP etalon established we can use this value when testing our

laser frequency locking program to convert the dither or drift seen in the laser peak position into frequency in MHz.

### 5.4.2 Stability of Laser Locking Program

Along with the calibration of the FSR covered in section 5.4.1, typical drifts of the CFP system and MBR frequency must be obtained in order to evaluate the performance of the laser frequency locking program. In order to establish the inherent errors associated to the CFP system and the programs acquisition and fitting protocol the EOM was employed as described in the previous section to create sidebands on the HeNe. These sidebands are absolutely locked in frequency with respects to the fundamental HeNe peaks that constitute the FSR. The frequency drift measured in this fashion is independent of frequency drift of the HeNe laser as any drift in the sideband frequency is exactly mirrored in the fundamental peaks that constitute the FSR. The frequency difference between carrier and sidebands is determined entirely by the RF generator. Once the FSR is locked any drift in the frequency of the HeNe will be identical to that of its EOM generated sideband. In this way any drift or uncertainty displayed by the sideband is that of the system. This drift will give us the lower error bound that the current system can attain for frequency drift. Our laser frequency locking program cannot produce lower frequency drifts than those inherent to the system. In order to obtain this lower bound the HeNe sideband position in units of FSR were logged over a period of 40 mins using the program. The positions were binned into a histogram and a normal distribution fitted to it as shown in Figure 5.8. The FWHM of the normal distribution is the quantity used to characterize of the drift of the laser position. From the normal distributions, the standard deviations  $\sigma$  are extracted and the FWHM computed according to the following equation [73]:

$$FWHM = 2\sqrt{2 \ln 2}\sigma \quad (5.12)$$

The drift of the HeNe sideband as described by the FWHM of the normal distribution as shown in Figure 5.8 is of  $1.411 \pm 0.004$  MHz over 40mins.

Now that we have determined the precision and inherent drift of our system using the sidebands, the stability of the MBR can be investigated. The MBR is set at 780nm and

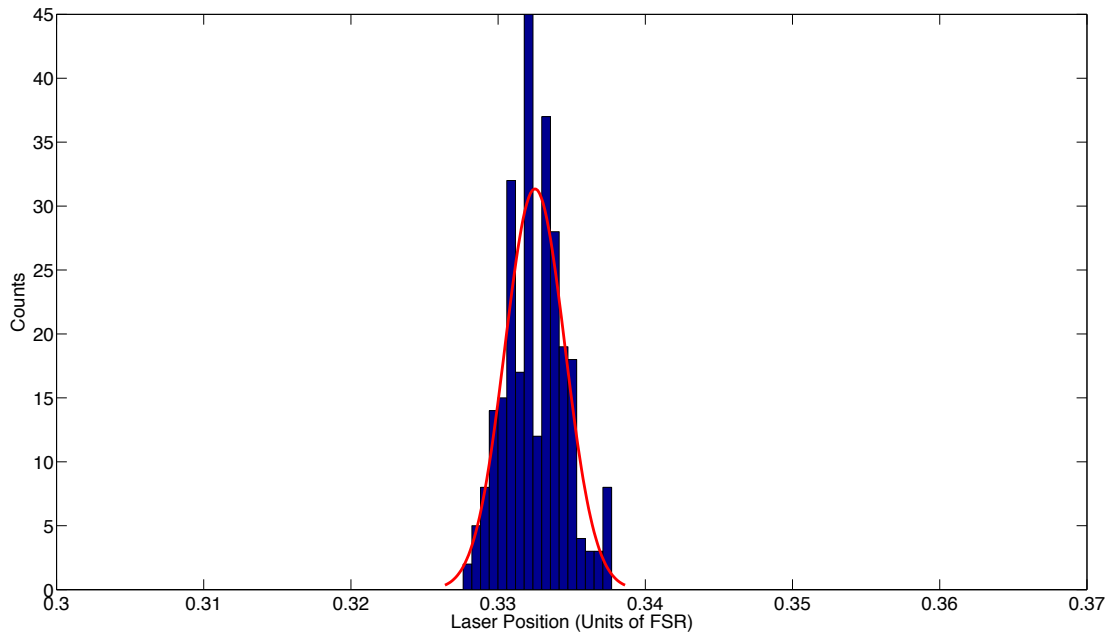


FIGURE 5.8: Histogram of the position of the HeNe sideband with the FSR locked along with its associated normal distribution. The FWHM of the normal distribution is found to be of  $1.411 \pm 0.004$  MHz over a period of 40mins.

locked to its internal cavity whilst the initial set of stability measurements are taken. To test the drift of the unlocked MBR, the laser frequency locking program was not engaged. Instead, with the FSR locked, the position of the MBR was tracked over a 40min period. The results of which are again binned and fitted to a normal distribution as shown in Figure 5.9. Whilst the drift of the HeNe sideband was mostly short term dither about a fixed position, the drift of the unlocked MBR peak is a long term smooth drift away from an initial position. This can be seen from the split distribution and larger FWHM seen in 5.9.

Important to note before being able to quote the drift of the MBR in MHz is that the distance between consecutive HeNe peaks as scanned by the PZT is of  $\lambda_{HeNe}/4$  from Eqn 5.1. This distance is the calibrated FSR of 300.2(8) MHz but as the MBR has a different wavelength, the  $\lambda_{MBR}/4$  distance between consecutive MBR peaks is different. Therefore the MBR laser frequency shift  $\Delta\nu_{MBR}$  is related to that of the HeNe reference laser  $\Delta\nu_{HeNe}$  by the following equation:

$$\Delta\nu_{MBR} = \frac{\lambda_{HeNe}}{\lambda_{MBR}} \Delta\nu_{HeNe} \quad (5.13)$$

In order to account for this a conversion factor  $C_F$  must be introduced such that  $C_F = \lambda_{HeNe}/\lambda_{MBR}$ . In order to obtain the FWHM of the MBR position distribution in MHz the following relation is employed:

$$FWHM = 2\sqrt{2\ln 2}\sigma C_F \quad (5.14)$$

The measured value of the FWHM for the unlocked MBR over a period of 40mins is of  $6.59 \pm 0.02\text{MHz}$ . This value is considerably larger than the one obtained for the HeNe sideband and illustrates the long term drift of the MBR laser and the need for the laser frequency locking program.

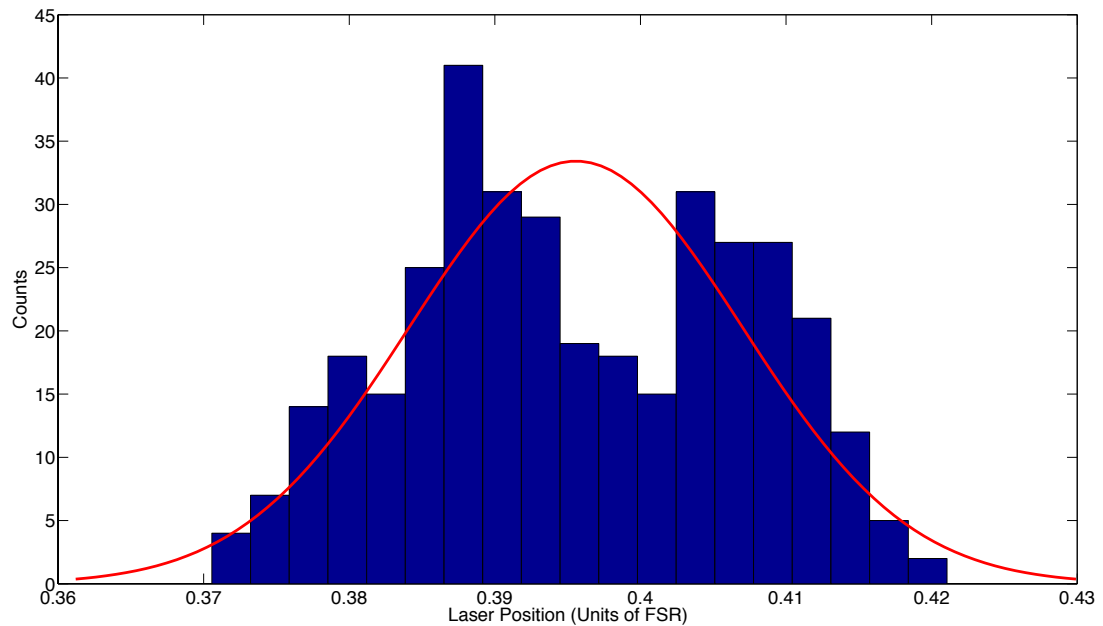


FIGURE 5.9: Histogram of the position of the unlocked MBR peak with the FSR locked along with its associated normal distribution. The FWHM of the normal distribution is found to be of  $6.59 \pm 0.02\text{MHz}$  over a period of 40mins.

Finally the laser frequency locking program is engaged and the MBR peak position tracked, the results of which are shown in Figure 5.10. The PI feedback loop previously described sends the voltage bias to the MBR bias to account for its long term drift. Employing Eqn 5.10 the FWHM of the normal distribution fitted to the MBR position can be obtained. It is found to be  $2.004 \pm 0.007\text{ MHz}$ , well below that of the drift associated with the unlocked MBR. In addition this is a deviation about a point as testifies the well fitting normal distribution. The uni-directional drift seen in the unlocked case that

leads to mode hopping has been suppressed successfully.

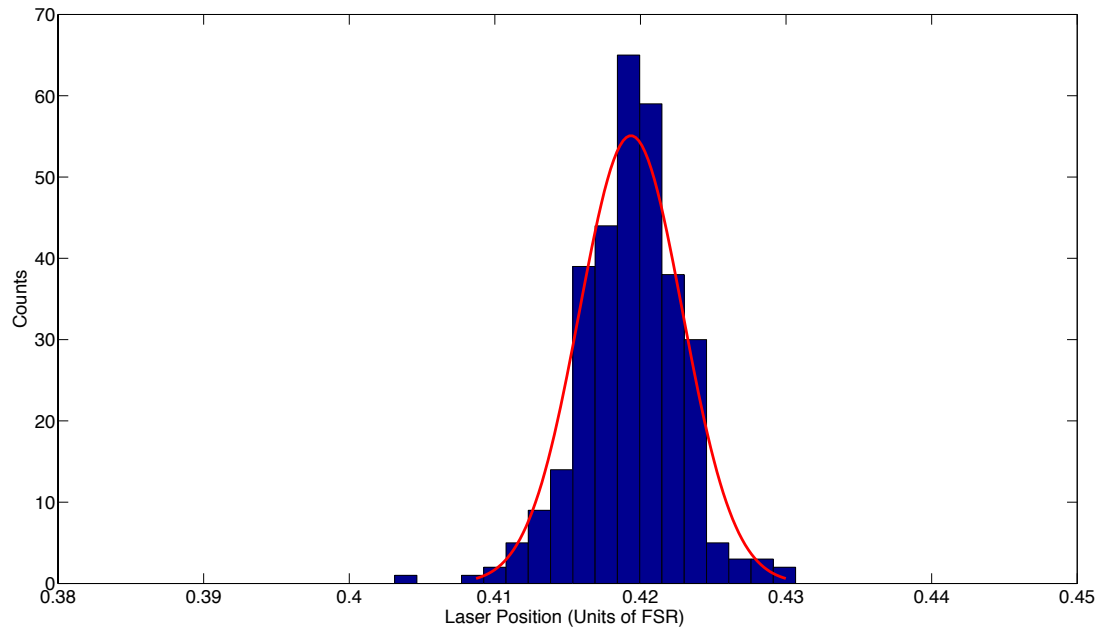


FIGURE 5.10: Histogram of the position of the locked MBR peak with the FSR locked along with its associated normal distribution. The FWHM of the normal distribution is found to be of  $2.004 \pm 0.007$  MHz over a period of 40mins.

### 5.4.3 Conclusion and Outlook

The CFP employed for laser stabilization was characterized and its FSR measured to be 300.2 (8) MHz using an innovative calibration employing EOM generated sidebands. The laser frequency locking program is found to vastly improve the long term stability of the MBR frequency by eliminating the long term uni-directional drift seen in the unlocked MBR frequency. It is found to possess a  $2.004 \pm 0.007$  MHz drift over a period of 40 mins, Less than a third of that displayed by the free running laser. The parameters of the PI feedback loop have only been subjected to a manual tuning. The parameters were altered whilst the system and lock were online and the output monitored in real time. The optimal PI tuning was then determined in this way, using trial and error in an effort to minimize both overshoot and oscillations about the set-point, both characteristic of mistuned feedback parameters. A more systematic tune can be achieved using the empirical Ziegler-Nichols method [74]. In this method a critical proportional gain constant  $K_p$  is

determined by increasing its value from zero until the output starts to visibly oscillate around the set-point with a constant amplitude. Once this state has been achieved  $K_p$  and period of oscillation  $T_p$  are used to determine the optimal proportional gain constants  $C_p$  and  $C_i$  for the proportional and integral controllers respectively. According to the Ziegler-Nichols method, for a PI controller:

$$C_p = 0.45K_p \quad (5.15a)$$

$$C_i = 1.2K_p/T_p \quad (5.15b)$$

The optimized parameters will improve the stability of the laser frequency and reduce the drift even further. Other avenues to improve laser stability would be the investigation of any non-linearities in the voltage ramp used to drive the PZT but also in the PZT's response to the voltage. These non-linearities affect the laser locking program and reduce its capacity to stabilize the excitation laser's frequency.

Finally the CFBS group has recently upgraded its laser system in order to improve its versatility, reliability and stability. The MBR pumped argon ion laser system described in Chapter 3 has been replaced by a M Squared Lasers Ltd, SolsTiS<sup>R</sup> CW Ti Sapphire Laser. The argon ion laser's power and stability have considerably deteriorated in the last couple of years of use by the CFBS group and so a new system was necessary in order to guarantee the groups future experimental operational capabilities. The upgraded system provides much improved stability and power. The new system boasts a fully integrated pump laser and local/remote control and monitoring via ethernet connection. In this way the laser wavelengths no longer needs to be manually changed by the experimenters when investigating different elements using laser spectroscopy. The new laser system's long term stability is yet to be tested with the laser frequency program described in this Chapter 5. New calibrations of the long term stability of the new system can be made using the laser frequency locking system and compared to those obtained for the previous system. Equally a new set of tuning parameters for the feedback loops must be obtained. Once theses calibrations and parameters have been undertaken the CFBS group has scheduled experimental runs this autumn to investigate Francium. An exciting time for the CFBS group.

# Bibliography

- [1] Joseph John Thomson. Xl. cathode rays. *The London, Edinburgh, and Dublin Philosophical Magazine and Journal of Science*, 44(269):293–316, 1897.
- [2] Joseph John Thomson. Xxiv. on the structure of the atom: an investigation of the stability and periods of oscillation of a number of corpuscles arranged at equal intervals around the circumference of a circle; with application of the results to the theory of atomic structure. *The London, Edinburgh, and Dublin Philosophical Magazine and Journal of Science*, 7(39):237–265, 1904.
- [3] Ernest Rutherford. Lxxix. the scattering of  $\alpha$  and  $\beta$  particles by matter and the structure of the atom. *The London, Edinburgh, and Dublin Philosophical Magazine and Journal of Science*, 21(125):669–688, 1911.
- [4] Hans Geiger and Ernest Marsden. On a diffuse reflection of the  $\alpha$ -particles. *Proceedings of the Royal Society of London. Series A, Containing Papers of a Mathematical and Physical Character*, 82(557):495–500, 1909.
- [5] Niels Bohr. I. on the constitution of atoms and molecules. *The London, Edinburgh, and Dublin Philosophical Magazine and Journal of Science*, 26(151):1–25, 1913.
- [6] Lester Aronberg. Note on the spectrum of the isotopes of lead. *The Astrophysical Journal*, 47:96, 1918.
- [7] Jenny E Rosenthal and G Breit. The isotope shift in hyperfine structure. *Physical Review*, 41(4):459, 1932.
- [8] Peter Brix and Hans Kopfermann. Zur isotopieverschiebung im spektrum des samariums. *Zeitschrift für Physik*, 126(3-4):344–364, 1949.

- [9] Albert A Michelson. Xxx. on the application of interference methods to spectroscopic measurements.—ii. *The London, Edinburgh, and Dublin Philosophical Magazine and Journal of Science*, 34(208):280–299, 1892.
- [10] Wolfgang Pauli. Zur frage der theoretischen deutung der satelliten einiger spektrallinien und ihrer beeinflussung durch magnetische felder. *Naturwissenschaften*, 12(37):741–743, 1924.
- [11] H Schüler and JE Keyston. Hyperfeinstrukturen und kernmomente des quecksilbers. *Zeitschrift für Physik*, 72(7-8):423–441, 1931.
- [12] Joseph Fraunhofer. Bestimmung des brechungs-und des farbenzerstreungsvermögens verschiedener glasarten, in bezug auf die vervollkommnung achromatischer fernröhre. *Annalen der Physik*, 56(7):264–313, 1817.
- [13] Daniel A Steck. Rubidium 87 d line data, 2001.
- [14] David Jeffrey Griffiths and Edward G Harris. *Introduction to quantum mechanics*, volume 2. Prentice Hall New Jersey, 1995.
- [15] Gordon Kemble Woodgate. Elementary atomic structure. 1970.
- [16] John David Jackson and John D Jackson. *Classical electrodynamics*, volume 3. Wiley New York etc., 1962.
- [17] R.W. Hasse and W.D. Myers. *Geometrical relationships of macroscopic nuclear physics*. Springer series in nuclear and particle physics. Springer-Verlag, 1988. ISBN 9783540175100. URL <http://books.google.ca/books?id=esvvAAAAMAAJ>.
- [18] C.A. Bertulani. *Nuclear Physics in a Nutshell*. In a Nutshell. Princeton University Press, 2007. ISBN 9781400839322. URL [http://books.google.ca/books?id=n51yJr4b\\_oQC](http://books.google.ca/books?id=n51yJr4b_oQC).
- [19] B Cheal and K T Flanagan. Progress in laser spectroscopy at radioactive ion beam facilities. *Journal of Physics G: Nuclear and Particle Physics*, 37(11):113101, 2010. URL <http://stacks.iop.org/0954-3899/37/i=11/a=113101>.
- [20] H. Ehrenreich and D. Turnbull. *Solid State Physics: Advances in Research and Applications Volume 46*. Solid state physics. Elsevier Science, 1992. ISBN 9780080865102. URL <http://books.google.ca/books?id=DFuogYn1VIUC>.

- [21] Pierre Jacquinot and Robert Klapisch. Hyperfine spectroscopy of radioactive atoms. *Reports on Progress in Physics*, 42(5):773, 1979.
- [22] EC Seltzer. K x-ray isotope shifts. *Physical Review*, 188(4):1916, 1969.
- [23] E Arimondo, M Inguscio, and P Violino. Experimental determinations of the hyperfine structure in the alkali atoms. *Reviews of Modern Physics*, 49(1):31, 1977.
- [24] Hendrik Brugt Gerhard Casimir. *On the interaction between atomic nuclei and electrons*. Springer, 1936.
- [25] R Neugart and G Neyens. Nuclear moments. In *The Euroschool Lectures on Physics with Exotic Beams, Vol. II*, pages 135–189. Springer, 2006.
- [26] J Billowes and P Campbell. High-resolution laser spectroscopy for the study of nuclear sizes and shapes. *Journal of Physics G: Nuclear and Particle Physics*, 21(6):707, 1995.
- [27] D Berdichevsky and F Tondeur. Nuclear core densities, isotope shifts, and the parametrization of the droplet model. *Zeitschrift für Physik A Atoms and Nuclei*, 322(1):141–147, 1985.
- [28] W Nörtershäuser, D Tiedemann, M Žáková, Z Andjelkovic, K Blaum, ML Bissell, R Cazan, GWF Drake, Ch Geppert, M Kowalska, et al. Nuclear charge radii of be 7, 9, 10 and the one-neutron halo nucleus be 11. *Physical review letters*, 102(6):062503, 2009.
- [29] AE Siegman. Lasers (university science, mill valley, calif., 1986). *Chap*, 13:663.
- [30] B Cheal, K Baczyńska, J Billowes, P Campbell, FC Charlwood, T Eronen, DH Forest, A Jokinen, T Kessler, ID Moore, et al. Laser spectroscopy of niobium fission fragments: first use of optical pumping in an ion beam cooler buncher. *Physical review letters*, 102(22):222501, 2009.
- [31] A Nieminen, P Campbell, J Billowes, DH Forest, JAR Griffith, J Huikari, A Jokinen, ID Moore, R Moore, G Tungate, et al. On-line ion cooling and bunching for collinear laser spectroscopy. *Physical review letters*, 88(9):094801, 2002.
- [32] Heinrich Gerhard Kuhn. Atomic spectra. 1969.

- [33] Heather J Lewandowski, DM Harber, Dwight L Whitaker, and EA Cornell. Simplified system for creating a bose–einstein condensate. *Journal of low temperature physics*, 132(5-6):309–367, 2003.
- [34] O.Shelbaya. An mcs based apparatus for collinear fast beam spectroscopy.
- [35] JE Sansonetti. Spectroscopic data for neutral francium (fri). *Journal of physical and chemical reference data*, 36(2):497–508, 2007.
- [36] Alan Corney. *Atomic and laser spectroscopy*. Clarendon Press Oxford, 1978.
- [37] E Mané, JA Behr, J Billowes, T Brunner, M Brodeur, F Buchinger, JE Crawford, J Dilling, S Ettenuer, CDP Levy, et al. Collinear laser spectroscopy with reverse-extracted bunched beams at triumf. *Hyperfine Interactions*, 199(1-3):357–363, 2011.
- [38] Gustav Kirchhoff and Robert Bunsen. Chemische analyse durch spectralbeobachtungen. *Annalen der Physik*, 186(6):161–189, 1860.
- [39] Arnold F Holleman. *Lehrbuch der anorganischen Chemie*. Walter de Gruyter, 1995.
- [40] Balraj Singh. Nuclear data sheets for a= 100. *Nuclear Data Sheets*, 109(2):297–516, 2008.
- [41] C Thibault, F Touchard, S Büttgenbach, R Klapisch, M de Saint Simon, HT Duong, P Jacquinet, P Juncar, S Liberman, P Pillet, et al. Hyperfine structure and isotope shift of the d 2 line of rb 7 6-9 8 and some of their isomers. *Physical Review C*, 23(6):2720, 1981.
- [42] Georges Audi, O Bersillon, J Blachot, and AH Wapstra. The nubase evaluation of nuclear and decay properties. *Nuclear Physics A*, 729(1):3–128, 2003.
- [43] Maria Goeppert Mayer. On closed shells in nuclei. ii. *Physical Review*, 75(12):1969–1970, 1949.
- [44] M Keim, E Arnold, W Borchers, U Georg, A Klein, R Neugart, L Vermeeren, RE Silverans, and Peter Lievens. Laser-spectroscopy measurements of  $^{87}\text{Rb}$  spins, moments and charge radii. *Nuclear Physics A*, 586(2):219–239, 1995.
- [45] F Buchinger, EB Ramsay, E Arnold, W Neu, R Neugart, K Wendt, RE Silverans, Peter Lievens, L Vermeeren, D Berdichevsky, et al. Systematics of nuclear ground

- state properties in sr 78–100 by laser spectroscopy. *Physical Review C*, 41(6):2883, 1990.
- [46] B Cheal, MD Gardner, M Avgoulea, J Billowes, ML Bissell, P Campbell, T Eronen, KT Flanagan, DH Forest, J Huikari, et al. The shape transition in the neutron-rich yttrium isotopes and isomers. *Physics Letters B*, 645(2):133–137, 2007.
- [47] K Baczynska, J Billowes, P Campbell, FC Charlwood, B Cheal, T Eronen, DH Forest, A Jokinen, T Kessler, ID Moore, et al. Nuclear spin determination of 100my by collinear laser spectroscopy of optically pumped ions. *Journal of Physics G: Nuclear and Particle Physics*, 37(10):105103, 2010.
- [48] VA Dzuba, WR Johnson, and MS Safronova. Calculation of isotope shifts for cesium and francium. *Physical Review A*, 72(2):022503, 2005.
- [49] Hans Kopfermann. Nuclear moments. 1958.
- [50] GP Barwood, P Gill, and WRC Rowley. Frequency measurements on optically narrowed rb-stabilised laser diodes at 780 nm and 795 nm. *Applied Physics B*, 53(3):142–147, 1991.
- [51] Gerhard Fricke, Herwig F Schopper, K Heilig, Hans Landolt, and Richard Börnstein. *Nuclear charge radii*. Springer, 2004.
- [52] E Mané, A Voss, JA Behr, J Billowes, T Brunner, F Buchinger, JE Crawford, J Dilling, S Ettenauer, CDP Levy, et al. First experimental determination of the charge radius of rb 74 and its application in tests of the unitarity of the cabibbo-kobayashi-maskawa matrix. *Physical review letters*, 107(21):212502, 2011.
- [53] T. Proctor. Measurements of an isomeric state in 98rb and a review on the nuclear properties of the rubidium isotope chain measured by laser spectroscopy.
- [54] Peter Möller, Arnold J Sierk, Ragnar Bengtsson, Hiroyuki Sagawa, and Takatoshi Ichikawa. Global calculation of nuclear shape isomers. *Physical review letters*, 103(21):212501, 2009.
- [55] R Rodriguez-Guzman, Pedro Sarriguren, and LM Robledo. Signatures of shape transitions in odd-a neutron-rich rubidium isotopes. *Physical Review C*, 82(6):061302, 2010.

- [56] O. Shelbaya. Laser spectroscopy of rare rubidium isotopes and development of data analysis software at triumph. Master's thesis, McGill, 2012.
- [57] G Lhersonneau, B Pfeiffer, R Capote, JM Quesada, H Gabelmann, and K-L Kratz. A  $k=3$  two-quasiparticle isomer in  $^{98}\text{Sr}$ . *Physical Review C*, 65(2):024318, 2002.
- [58] Klaus Blaum, Jens Dilling, and Wilfried Nörtershäuser. Precision atomic physics techniques for nuclear physics with radioactive beams. *Physica Scripta*, 2013(T152):014017, 2013.
- [59] P Bohlouli-Zanjani, K Afrousheh, and JDD Martin. Optical transfer cavity stabilization using current-modulated injection-locked diode lasers. *Review of scientific instruments*, 77(9):093105, 2006.
- [60] Craig J Sansonetti. Precise measurements of hyperfine components in the spectrum of molecular iodine. *JOSA B*, 14(8):1913–1920, 1997.
- [61] Ch Salomon, D Hils, and JL Hall. Laser stabilization at the millihertz level. *JOSA B*, 5(8):1576–1587, 1988.
- [62] TM Niebauer, James E Faller, HM Godwin, John L Hall, and RL Barger. Frequency stability measurements on polarization-stabilized he-ne lasers. *Applied optics*, 27(7):1285–1289, 1988.
- [63] WZ Zhao, JE Simsarian, LA Orozco, and GD Sprouse. A computer-based digital feedback control of frequency drift of multiple lasers. *Review of scientific instruments*, 69(11):3737–3740, 1998.
- [64] M Vaughan. *The Fabry-Perot interferometer: history, theory, practice and applications*. CRC press, 1989.
- [65] Michael Hercher. The spherical mirror fabry-perot interferometer. *Applied Optics*, 7(5):951–966, 1968.
- [66] K Fukamichi, M Kikuchi, S Arakawa, and T Masumoto. Invar-type new ferromagnetic amorphous fe-b alloys. *Solid State Communications*, 23(12):955–958, 1977.
- [67] H-J Pan, P Ruan, H-W Wang, and F Li. Confocal fabry-perot interferometer for frequency stabilization of laser. *Laser Physics*, 21(2):336–339, 2011.

- 
- [68] JR Johnson. A high resolution scanning confocal interferometer. *Applied optics*, 7 (6):1061–1072, 1968.
- [69] Gonzalo Hernández. *Fabry-Perot Interferometers*, volume 3. Cambridge University Press, 1988.
- [70] *NI 622x Specifications*. National Instruments, June 2007.
- [71] Karl J ström and Tore Hägglund. *Pid controllers: theory, design, and tuning*. Instrument Society of America, Research Triangle Park, NC, 1995.
- [72] ADRIANUS KOWEL. Acousto-optics-a review of fundamentals. *Proceedings of the IEEE*, 69(1), 1981.
- [73] Eric W Weisstein. Gaussian function. *From MathWorld—A Wolfram Web Resource*. <http://mathworld.wolfram.com/GaussianFunction.html>, 1999.
- [74] JG Ziegler and NB Nichols. Optimum settings for automatic controllers. *trans. ASME*, 64(11), 1942.